Forced and unforced decadal behavior of the interhemispheric SST contrast during the instrumental period (1881–2012)

Forced and unforced decadal behavior of the interhemispheric SST contrast during the instrumental period (1881–2012): contextualizing the abrupt shift around 1970

Andrew R. Friedman[1], Gabriele C. Hegerl[1], Andrew Schurer[1], Shih-Yu Lee[2], Wenwen Kong[3], Wei Cheng[4], and John C. H. Chiang[3]

Resubmission to *Journal of Climate*, 6 December 2019

[1]School of Geosciences, University of Edinburgh, Edinburgh, United Kingdom

[2]Research Center for Environmental Changes, Academia Sinica, Taipei, Taiwan

[3]Department of Geography, University of California, Berkeley, California, USA

[4]Joint Institute for the Study of the Atmosphere and Ocean, University of Washington, USA

Corresponding author: Andrew R. Friedman. Crew Building, The King's Buildings, Alexander Crum Brown Road, Edinburgh EH9 3FF, United Kingdom. <andrew.friedman@ed.ac.uk>

ORCID ID https://orcid.org/0000-0001-6994-2037

Early Online Release: This preliminary version has been accepted for publication in *Journal of Climate*, may be fully cited, and has been assigned DOI 10.1175/JCLI-D-19-0102.1. The final typeset copyedited article will replace the EOR at the above DOI when it is published.

Abstract

The sea surface temperature (SST) contrast between the northern hemisphere (NH) and southern hemisphere (SH) influences the location of the intertropical convergence zone (ITCZ) and the intensity of the monsoon systems. This study examines the contributions of external forcing and unforced internal variability to the interhemispheric SST contrast in HadSST3 and ERSSTv5 observations, and 10 models from the Coupled Model Intercomparison Project Phase 5 (CMIP5) from 1881–2012. Using multimodel mean fingerprints, a significant influence of anthropogenic, but not natural, forcing is detected in the interhemispheric SST contrast, with the observed response larger than that of the model mean in ERSSTv5. The forced response consists of asymmetric NH–SH SST cooling from the mid 20th century to around 1980, followed by opposite NH–SH SST warming. The remaining best-estimate residual or unforced component is marked by NH–SH SST maxima in the 1930s and mid 1960s, and a rapid NH–SH SST decrease around 1970. Examination of decadal shifts in the observed interhemispheric SST contrast highlights the shift around 1970 as the most prominent from 1881–2012. Both NH and SH SST variability contributed to the shift, which appears not to be attributable to external forcings. Most models examined fail to capture such large-magnitude shifts in their control simulations, though some models with high interhemispheric SST variability are able to produce them. Large-magnitude shifts produced by the control simulations feature disparate spatial SST patterns, some of which are consistent with changes typically associated with the Atlantic Meridional Overturning Circulation (AMOC).

Accepted for publication in *Journal of Climate*. DOI 10.1175/JCLI-D-19-0102.1.

1. Introduction

The north–south interhemispheric surface temperature contrast is an important influence on the location of the intertropical convergence zone (ITCZ) and the strength of the African and Asian monsoons (Folland et al. 1986; Mantsis and Clement 2009; Chiang and Friedman 2012; Hwang et al. 2013; Sun et al. 2013; Schneider et al. 2014); as well as the extratropical circulation (Xue et al., 2018). Previous studies have identified the role of different forcings that have contributed to changes in the interhemispheric temperature contrast over the instrumental period (Drost and Karoly, 2012; Friedman et al., 2013). For combined land and ocean surface temperatures, stronger northern hemisphere (NH) than southern hemisphere (SH) warming is a robust transient climate response to greenhouse gas (GHG) forcing, largely due to the greater NH landmass extent and thus smaller thermal inertia (Stouffer et al. 1989; Xu and Ramanathan 2012). Arctic amplification processes also contribute to greater transient NH warming (Serreze and Barry, 2011). In contrast, the transient warming in the Southern Ocean is limited by upwelling, the thermal isolation of Antarctica from the Antarctic Circumpolar Current, and the Southern Ocean meridional overturning circulation (Hutchinson et al., 2013; Marshall et al., 2014; Armour et al., 2016). Northward heat transport by the Atlantic Meridional Overturning Circulation (AMOC) is the main cause of the mean positive NH–SH temperature contrast (Feulner et al., 2013; Kang et al., 2014), and a decreasing AMOC is projected to weaken the interhemispheric temperature contrast in moderate-emissions future climate projections (Feulner et al., 2013).

Due to their sources mainly in the NH and their relatively short atmospheric residence times, anthropogenic aerosol emissions contribute to North Atlantic cooling and a decreased NH–SH interhemispheric temperature contrast (Kiehl and Briegleb 1993; Rotstayn and Lohmann 2002;

Accepted for publication in *Journal of Climate*. DOI 10.1175/JCLI-D-19-0102.1.

Chang et al. 2011; Allen et al. 2015; Chung and Soden 2017). Though the magnitude of mid-20th century aerosol forcing remains uncertain (Stevens, 2015; Kretzschmar et al., 2017; Booth et al., 2018), historical climate model simulations suggest that the positive NH–SH surface temperature imbalance from GHG forcing overtook the aerosol-related NH–SH decrease around 1980 (Drost and Karoly, 2012; Friedman et al., 2013; Wilcox et al., 2013; Undorf et al., 2018), with uncertainty on exact timing due to internal variability and intermodal differences (Schurer et al., 2018). This reflects North American and European clean air legislation in the 1970s and continued GHG emissions. Asian sulfate aerosol emissions have also steadily increased since the 1950s, though present-day global emissions do not exceed 1970s estimates (Lamarque et al., 2010; Hoesly et al., 2018). Asian and African black carbon aerosol emissions have also increased during this period; their overall radiative forcing is uncertain but estimated to be positive, spatially and less hemispherically asymmetric compared to sulfate (Bond et al., 2013; Boucher et al., 2013; Wang et al., 2016). Future anthropogenic aerosol declines are projected to expose even larger NH warming in the coming decades (Rotstayn et al. 2013; Rotstayn et al. 2015). Another interhemispheric forcing is stratospheric ozone depletion, which may have stalled SH high-latitude warming (Marshall et al., 2014).

Despite the above progress in physical understanding of the interhemispheric temperature contrast, key questions remain about the roles of forced and unforced interhemispheric temperature variability during the instrumental period. Notably, studies have identified a shift in the interhemispheric temperature difference from the late 1960s through the early 1970s, which had wide-ranging hydrological impacts particularly on Asian and West African monsoon rainfall (Baines and Folland, 2007; Dima and Lohmann, 2010; Thompson et al., 2010; Liu and Chiang, 2012). Thompson et al. (2010) do not find any instrumental SST biases at the time of the shift,

Accepted for publication in *Journal of Climate*. DOI 10.1175/JCLI-D-19-0102.1.

and use an analytical adjustment methodology to show the drop was unrelated to El Niño / Southern Oscillation (ENSO) fluctuations, volcanic eruptions, or advection by wintertime atmospheric circulation. Due to the rapid timescale of the drop and association with a rapid freshening known as the Great Salinity Anomaly (Dickson et al., 1988), it has been proposed that the interhemispheric shift was caused by internal ocean variability, notably a shift in the AMOC (Dima and Lohmann, 2010; Thompson et al., 2010), possibly as part of a longer-term decline over the 20th century driven by Greenland and Arctic meltwater (Rahmstorf et al., 2015; Caesar et al., 2018). However, this period also coincides with strong sulfate aerosol forcing (Terray, 2012; Friedman et al., 2013; Wilcox et al., 2013; Hodson et al., 2014; Allen et al., 2015). Since the magnitude of interhemispheric temperature shifts has not been explicitly quantified, it is difficult to express how unusual the 1970 shift was compared to earlier periods, or if climate models are able to produce comparable shifts. At the millennial timescale, there have been indications that climate models may underestimate interhemispheric temperature variability in paleoclimate reconstructions, through some of the discrepancies may be due to data uncertainties (Neukom et al., 2014, 2018).

This study aims to characterize the decadal variability of the interhemispheric temperature contrast (focusing on SST only) in a quantitative framework so that the magnitude of the 1970 shift and other changes can be evaluated more rigorously. We employ a regression-based climate change detection and attribution approach (Hegerl et al. 1997; Allen and Stott 2003) to extract the forced and unforced components of the interhemispheric SST contrast. We also examine NH and SH SST separately to understand their respective contributions to interhemispheric SST variability. Furthermore, we quantify decadal interhemispheric SST shifts using running linear trends and examine the spatial patterns associated with the largest-magnitude trends, analogous

Accepted for publication in *Journal of Climate*. DOI 10.1175/JCLI-D-19-0102.1.

105 to the approach used in recent studies to quantify the early-2000s global mean surface
106 temperature slowdown or *hiatus* (Meehl et al. 2011; Schurer et al. 2015; Marotzke and Forster
107 2015; Medhaug et al. 2017).

108 The paper is organized as follows: In **Section 2**, we present the datasets and simulations
109 investigated. **Section 3** describes the characteristics of decadal interhemispheric SST variability.
110 The detection and attribution analysis is applied to the interhemispheric SST contrast in **Section**
111 **4**. The separate NH and SH components of interhemispheric SST variability are examined in
112 **Section 5. Section 6** focuses on decadal shifts in the interhemispheric SST contrast. Finally,
113 **Section 7** concludes with the implications of our work plus some open questions.
114

115 **2. Data and models**

116 We define the interhemispheric SST contrast anomaly as the anomaly of mean NH minus
117 mean SH SST; the annual mean is shown in **Figure 1a** (top). We examine SST monthly fields
118 from the Met Office Hadley Center SST dataset (HadSST3) (Kennedy et al. 2011a, 2011b) and
119 the NOAA Extended Reconstructed SST dataset, version 5 (ERSSTv5) (Huang et al., 2017).
120 HadSST3 and ERSSTv5 are both constructed from *in situ* data using much of the same sources,
121 but apply different quality control, bias corrections, and homogenization. One difference is that
122 ERSSTv5 infills missing data using empirical orthogonal teleconnections, whereas the HadSST3
123 data are not infilled. Annual means are taken from December–November, which better fit
124 climatological seasons and the ENSO annual cycle, and are calculated from 3-month seasonal
125 means (constructed if there is at least one month of data): December–February, March–May,
126 June–August, and September–November.

Accepted for publication in *Journal of Climate*. DOI 10.1175/JCLI-D-19-0102.1.

Previous studies on the interhemispheric temperature contrast have often examined the combined land surface and SST interhemispheric temperature contrast (Drost and Karoly 2012; Friedman et al. 2013; Feulner et al. 2013; Wilcox et al. 2013). In comparison to the interhemispheric SST contrast, the interhemispheric contrast in land surface temperature, shown using the Climate Research Unit database (CRUTEM4) (Morice et al., 2012) and the NASA GISS Surface Temperature Analysis (GISTEMP) (Hansen et al., 2010) (250 km smoothing version) (**Figure 1a,** bottom), has larger interannual variability and a stronger long-term trend. As our focus is decadal variability, we hereafter investigate the interhemispheric SST contrast. While using SST minimizes the direct response of the land surface, we still expect some contribution from advection from land, especially over the NH (Thompson et al., 2009).

We also examine output from the Coupled Model Intercomparison Project Phase 5 (CMIP5) (Taylor et al. 2012), listed in **Table 1**. We select all model realizations for which both historical natural forcing (solar and volcanic, referred to as historicalNat) and the corresponding historical all-forcing (natural and anthropogenic, including GHGs, aerosols, ozone, and land use; referred to as historical) experiments are available from 1881–2012 to allow the longest possible period for the detection and attribution analysis. In total, 36 historical and historicalNat realizations from 10 different models are investigated. For 6 models, output was available from the historical or the historical extension (historicalExt) experiments from 2006–2012. For 4 models (IPSL-CM5A-LR, IPSL-CM5A-MR, CSIRO-Mk3-6-0, and one realization of HadGEM2-ES), the historical experiments end in 2005, so the Representative Concentration Pathway 4.5 (RCP4.5) experiment output (Vuuren et al., 2011) is used from 2006-2012.

We investigate SST from the corresponding pre-industrial control (piControl) runs of each CMIP5 model, whose lengths are also indicated in **Table 1**. Control simulations from two

Accepted for publication in *Journal of Climate*. DOI 10.1175/JCLI-D-19-0102.1.

150 additional models, NCAR CCSM4 and GFDL-CM3, are also examined in some analyses.
151 Though model drift has been found to affect some variables in CMIP5 models (Sen Gupta et al.,
152 2013), our results for the interhemispheric SST contrast are not affected by linear detrending of
153 the control runs (not shown).
154 The 2°x2° ERSSTv5 data and differing-resolution CMIP5 model output are interpolated onto
155 the 5°x5° HadSST3 grid. In computing hemispheric means, the datasets and models are masked
156 where HadSST3 contains no data in more than 15 of the first 60 years of the study (1881–1940),
157 shown in **Figure 1b**. [The land surface temperature data in **Figure 1a** (bottom) are masked using
158 a similar threshold based on the 1881–1940 CRUTEM4 coverage]. Hemispheric means are
159 calculated poleward of 5° latitude, as modes of interhemispheric SST variability are generally
160 not centered directly on the equator (Servain et al., 1999; Xie and Carton, 2004; Baines and
161 Folland, 2007).
162
163 **3. Observed and modeled interhemispheric SST variability**
164 As our focus is on decadal and multidecadal variability, we apply a 3-year running mean to
165 the annual data to suppress high-frequency variations such as ENSO (Wang et al. 2012; Dai
166 2013). The 3-year mean 1881-2012 observational interhemispheric SST anomaly time series are
167 shown in **Figure 1c**, along with those of the CMIP5 historical realizations and their ensemble
168 mean. The observational datasets are highly correlated (r=0.92), and generally remain within the
169 envelope of the historical simulations. The ensemble mean has a long-term negative trend until
170 around 1980 followed by a rebound, similar to the combined interhemispheric land and SST
171 difference due to opposing GHG and anthropogenic aerosol forcings (Friedman et al. 2013;
172 Wilcox et. al. 2013) albeit with a smaller trend since 1980. The amplitude of the ensemble mean

Accepted for publication in *Journal of Climate*. DOI 10.1175/JCLI-D-19-0102.1.

variations is expectedly smaller than that of the observations; the latter show a rapid north–south increase in the 1920s and north–south decrease from the late-1960s to early 1970s.

The 1881–2012 standard deviation of the 3-year mean interhemispheric SST contrast of the observations and historical simulations is shown in **Figure 1d**. The standard deviation of ERSSTv5 (0.13°C) is larger than that of HadSST3 (0.12°C); both are larger than the multimodel mean of standard deviations (0.11°C), though still within the inter-model range. An outlier is GISS-E2-H, whose standard deviations cluster between 0.07°C and 0.08 °C. The single-realization models (particularly bcc-csm1-1) also have low standard deviations, though we would need more realizations to evaluate their spread. Similar results are found with further smoothing, with a relatively larger spread of model standard deviations (not shown).

The spatial patterns corresponding to the interhemispheric SST contrast in observations are shown in **Figures 2a** and **2c**, obtained by ordinary least squares (OLS) regression of the 3-year mean gridded observations onto the interhemispheric SST time series from 1881-2012. Slope significance is evaluated using a 2-tailed *t*-test, adjusting for temporal autocorrelation by increasing the regression standard error by a factor of $\sqrt{3}$ assuming 1 degree of freedom for every 3 years of length (Santer et al., 2000; Biasutti et al., 2008). We additionally apply a False Discovery Rate (FDR) procedure to test for field significance (Genovese et al., 2002; Wilks, 2016), stippling the gridpoints with *p*-values satisfying the FDR criterion $\alpha_{FDR} = 0.05$. Both datasets have prominent significant positive slopes over the subpolar North Atlantic and significant negative slopes in the extratropical South Atlantic and South Indian oceans. ERSSTv5 has more significant gridboxes, presumably due to its reduced spatial noise. Negative Indian Ocean slopes extend into the NH, similar to the interhemispheric SST mode in Parker et

Accepted for publication in *Journal of Climate*. DOI 10.1175/JCLI-D-19-0102.1.

al. (2007). There are also positive slopes in the mid-latitude North Pacific, albeit not significant in either dataset.

Figure 2e shows the 1881-2012 ensemble mean spatial pattern of the 3-year mean CMIP5 historical interhemispheric SST contrast, calculated as the ensemble mean of the regression slopes of each gridded realization's SST field onto its own interhemispheric SST contrast time series (the thin lines in **Figure 1c**). The slopes are stippled where at least 30 of the 36 realizations agree on the sign of the slope. In contrast to the observations, the strongest amplitudes and model agreement are in the mid-latitude North Pacific, with maximum slopes over the Kuroshio extension. The models show consistent negative slopes in the extratropical SH, particularly the mid-latitude Atlantic and Indian oceans around 40°–45°S.

To illustrate the hydrologic impacts of interhemispheric SST variability, we show the spatial patterns of tropical rainfall associated with the interhemispheric SST contrast. **Figures 2b** and **2d** show the regression slopes of 3-year mean rainfall over land using the Global Precipitation Climatology Center (GPCC) 2.5° spatially-infilled full data monthly product, version 2018 (Becker et al. 2013; Schneider et al. 2018) onto the interhemispheric SST contrast. The observed slopes are calculated from 1930–2012 due to insufficient gauge coverage beforehand (Polson et al. 2016). Slopes are stippled where significant at $p<0.05$ using a 2-tailed *t*-test, adjusted for temporal autocorrelation and applying the FDR procedure similarly as the SST data in **Figures 2a** and **2c**. The right panels show the zonal mean slopes. **Figure 2f** shows the 1930-2012 ensemble mean slope of CMIP5 historical precipitation over land and ocean regressed onto the interhemispheric SST contrast, with the precipitation fields regridded onto a common 2.5° grid. Stippling indicates sign agreement of at least 30 of 36 realizations as in **Figure 2e**. The zonal

Accepted for publication in *Journal of Climate*. DOI 10.1175/JCLI-D-19-0102.1.

mean slopes in **Figure 2f** are shown both globally and for land regions only (masked to the GPCC grid), with the distribution of the middle 30 realizations indicated.

Both the observations and the models show displacement of tropical rainfall into the warmer SST hemisphere (Chung and Ramanathan, 2007; Chiang and Friedman, 2012; Sun et al., 2013), with observational slope significance and high model agreement found in the ITCZ and monsoon regions, emphasizing the strong imprint of the interhemispheric SST contrast on these rainfall features. However, almost all the realizations underestimate the zonal mean slope magnitudes in northern tropical land region around 10°N (largely reflecting Africa), consistent with larger-magnitude observed 20th century changes compared to most CMIP3 and CMIP5 models (Hwang et al., 2013; Polson et al., 2014; Hegerl et al., 2015).

4. Attribution of interhemispheric SST variability to forcing

In this section, we conduct a detection and attribution analysis to identify the forced components of the 3-year running mean interhemispheric SST contrast shown above.

4.1 Detection and attribution methodology

Detection and attribution provides a rigorous framework to separate the components of observed climate changes driven by external forcing and internal variability (e.g. Hegerl et al. 1997; Allen and Stott 2003). A typical assumption of regression-based detection and attribution studies such as used here is that the spatiotemporal response pattern of an external forcing is much better known than the response magnitude (Bindoff et al., 2013). Here, we apply total least squares (TLS) regression for detection and attribution of the interhemispheric SST contrast (Allen and Stott 2003). We use multimodel ensemble mean fingerprints, which have often been

Accepted for publication in *Journal of Climate*. DOI 10.1175/JCLI-D-19-0102.1.

found to perform better than any individual model (Knutti et al. 2010; Hegerl and Zwiers 2011), though may underestimate the role of model uncertainty (Schurer et al., 2018). Equal weight is given to each of the 36 realizations in constructing the multimodel ensemble mean. Calculating the mean over the available simulations rather than among individual models results in a greater signal-to-noise ratio, though it means that some models are given greater weight due to having more realizations.

We apply a two-signal analysis with historical and historicalNat fingerprints to detect net anthropogenic forcing, which has been found to be more robust than detecting aerosol and GHG forcing separately (Bindoff et al. 2013; Jones et al. 2016). The observations and fingerprints are shown in **Figure 3a**. As in Schurer et al. (2013), the fingerprints are not optimized. The scaling coefficients β_1 and β_2, which determine the magnitude of the fingerprints from observations, are calculated as follows:

$$y = \beta_1(X_{historicalNat} - \varepsilon_{historicalNat}) + \beta_2(X_{historical} - \varepsilon_{historical}) + \varepsilon_{obs} \quad , \quad (1)$$

where y is the observed interhemispheric SST contrast time series of length L (132 years excluding endpoints due to smoothing: 130 years); $X_{historicalNat}$ and $X_{historical}$ are the length-L multimodel mean fingerprints; $\varepsilon_{historicalNat}$ and $\varepsilon_{historical}$ are the length-L internal variability of each fingerprint; and ε_{obs} is the unforced residual variability. We assume that taking the mean over n ensemble members (36 realizations) reduces the internal variability by a factor of $\sqrt{n}$.

We rearrange β_1 and β_2 into natural (β_{Nat}) and anthropogenic (β_{Ant}) scaling coefficients, as described in Tett et al. (2002):

$$\beta_{Nat} = \beta_1 + \beta_2 \quad , \quad (2)$$

$$\beta_{Ant} = \beta_2 \quad , \quad (3)$$

Accepted for publication in *Journal of Climate*. DOI 10.1175/JCLI-D-19-0102.1.

We construct the 5-95% confidence intervals accounting for uncertainty in the internal variability of β_{Nat} and β_{Ant} by adding 16,000 random L-year samples from the control simulations onto the noise-reduced fingerprints and observations. For each iteration, we select 3 segments without replacement from the 42 non-overlapping 132-year segments available from the 10 control simulations corresponding to the fingerprints (**Table 1**), taking 3-year means (and excluding endpoints). The best-estimate coefficients and 5–95% confidence intervals are shown in **Table 2a**. Anthropogenic forcing is detected at the 5% one-sided significance level, whereas natural forcing is not significantly detectable. The best-estimate values of β_{Ant} greater than the multimodel mean (scaling of 1) suggest a larger response to anthropogenic forcing in observations than in models, particularly for ERSSTv5 where the multimodel mean is outside the 5–95% uncertainty range.

4.2 Forced and unforced components of the interhemispheric SST contrast

The best-estimate 3-year mean noise-reduced, or forced, component of y, $\tilde{y}$, is shown for HadSST3 in **Figure 3b** and ERSSTv5 in **Figure 3c**, with the 5%-95% confidence intervals constructed from the 16,000 random samples from the control runs. The anthropogenic and natural contributions to the forced components are also shown; the anthropogenic component is calculated by subtracting historicalNat from historical component; see **Equations (2)-(3)**. The anthropogenic component dominates the forced response for both datasets. The forced signal consists of a negative trend to around 1980 followed by a partial recovery. The negative trend is overlaid with an increase from around 1920 to 1950.

The best-estimate unforced residual or effective residual time series is estimated as follows:

Accepted for publication in *Journal of Climate*. DOI 10.1175/JCLI-D-19-0102.1.

$$\hat{\varepsilon}_{obs} = \frac{(\gamma - \beta_1 X_{historicalNat} - \beta_2 X_{historical})}{\sqrt{1 + \beta_1^2/n + \beta_2^2/n}}$$

, (4)

where the scaling factor in the denominator is applied to account for the small component of internal variability in the fingerprints (Schurer et al. 2015). We use both β_1 and β_2 in **Equation (4)** since physically we expect some contribution from both natural and anthropogenic forcing types of forcing, even though natural forcing is not found to be significant. The best-estimate residual time series (**Figure 3d**) has prominent north-south maxima in the 1930s and mid 1960s, with the latter followed by a rapid north-south decrease to the early 1970s. We will further examine these decadal changes in **Section 6**.

Figure 3e shows the best-estimate residual standard deviations along with those of the control segments (shown in purple). The best-estimate observational residuals are within the control simulation range, suggesting consistency in magnitude between the internal variability of the observations and the models. For example, the GISS-E2-H control simulation variability is more consistent in magnitude to the observational residuals than the GISS-E2-H historical variability compared to observations (**Figure 1d**). Also shown are the best-estimate residuals estimated from applying the detection and attribution methodology to each historical realization, described in the **Appendix** (shown in black). Note that this estimate of the internal variability includes an unknown forced component of each model which differs from the multimodel mean fingerprint. However, the historical best-estimate residual variability is also within the range of the control simulations (with both larger and smaller magnitudes), indicating that the multimodel mean fingerprints reasonably capture much of the forced variability in the individual models.

Accepted for publication in *Journal of Climate*. DOI 10.1175/JCLI-D-19-0102.1.

5. Northern and southern components of the interhemispheric SST contrast

Building on the previous section, we apply a detection and attribution analysis to NH and SH SST separately. The NH and SH fingerprints and observations are shown in **Figures 4a**–**4b**. Both hemisphere observations show a long-term positive trend after cooling from 1881 to around 1910. NH SST shows strong warming from around 1910–1940, described as early 20th century warming (Hegerl et al., 2018), followed by a slight decrease to around 1980, then strong warming until 2012. SH SST has a short-term increase around WWII, followed by relatively steady warming. ERSSTv5 and HadSST3 have the largest overall differences following WWII in the SH, with ERSSTv5 lower by about 0.2°C in the early 1950s (**Figure 4b**), potentially related to differences in bias corrections for the transition from bucket to engine room intakes (Kennedy 2014; Huang et al. 2017).

Using the methodology described in **Section 4.1**, we obtain the best-estimate scaling coefficients and 5–95% confidence intervals, shown in **Table 2b**. Note that our NH and SH detection and attribution analysis differs from some studies in which different indices or regions are combined when calculating scaling coefficients, such as Schurer et al. (2018). We choose this approach to extract the maximum forced variability in each hemisphere, though this allows for different scaling factors across the equator.

Anthropogenic forcing is detected at the 5% one-sided significance level in both the NH and SH. Natural forcing is detected in both hemispheres for HadSST3 (with β_{Nat} <1), but not in ERSSTv5. In both datasets, the best-estimate values of β_{Ant} are greater than 1 for both hemispheres, with the multimodel mean outside the 5–95% range for the SH. The best-estimate hemispheric forced components (**Figures 4c**-**4d**) are dominated by an upward trend from GHG

Accepted for publication in *Journal of Climate*. DOI 10.1175/JCLI-D-19-0102.1.

forcing, with aerosol-related NH cooling from 1950-1970 (Wilcox et al., 2013; Allen et al., 2015; Undorf et al., 2018).

The best-estimate residual NH and SH time series, $\hat{\varepsilon}_{obs\_NH}$ and $\hat{\varepsilon}_{obs\_SH}$, are calculated similarly to **Equation (4)** (**Figures 4e-4f**). As expected, the best-estimate residual interhemispheric SST contrast, $\hat{\varepsilon}_{obs}$ from **Equation (4)**, is very strongly correlated with the difference of $\hat{\varepsilon}_{obs\_NH}$ and $\hat{\varepsilon}_{obs\_SH}$ (HadSST3: r=0.98; ERSSTv5: r=0.93). The observed cooling from 1881 to around 1910 is present in both $\hat{\varepsilon}_{obs\_NH}$ and $\hat{\varepsilon}_{obs\_SH}$; likewise, much of the early 20th century NH warming, as $\hat{\varepsilon}_{obs\_NH}$ warms relatively steadily from 1910-1940 and later undergoes a decrease in the late 1960s. $\hat{\varepsilon}_{obs\_SH}$ increases rapidly in the late 1930s, then drops in the 1940s followed by decadal-scale variations, with minima in the mid-1960s and after the early 2000s. Both $\hat{\varepsilon}_{obs\_NH}$ and $\hat{\varepsilon}_{obs\_SH}$ have large standard deviations compared to the control simulations and the best-estimate NH and SH historical residuals (calculated following the **Appendix; Figure 4g**). $\hat{\varepsilon}_{obs\_NH}$ and $\hat{\varepsilon}_{obs\_SH}$ are also more positively correlated (HadSST3: r=0.63; ERSSTv5: r=0.62) than any of the control segments or historical residuals (**Figure 4h**). [This is not the case for the direct NH and SH SST observations, whose standard deviations and correlation are within the range of the historical realizations (not shown)]. The strong amplitude and correlation of the observed NH and SH best-estimate residuals suggest that the effect of forcing has been incompletely removed using the multimodel mean regression. The discrepancy may also be partly due to errors in observations or incorrect climate model decadal variability.

6. Decadal shifts in the interhemispheric SST contrast

In this section, we examine decadal shifts in the interhemispheric SST contrast. Several methodologies for identifying climate shifts exist (Overland et al., 2008). Here, we examine

Accepted for publication in *Journal of Climate*. DOI 10.1175/JCLI-D-19-0102.1.

running linear trends (Trottini et al., 2015), which have been typically used to quantify the early-2000s global mean surface temperature slowdown (Meehl et al. 2011; Schurer et al. 2015; Marotzke and Forster 2015; Medhaug et al. 2017). As our focus is on decadal-scale shifts, we examine 9-year running OLS trends applied to the 3-year running mean time series. Similar results are obtained using running trend lengths of 7 to 13 years (not shown).

6.1 1970 and 1920s shifts

Figure 5a shows the 3-year mean interhemispheric SST contrast along with the respective 9-year running trends. In both observational datasets, the largest-magnitude trend is the rapid drop centered around 1970, consistent with previous qualitative identification (Dima and Lohmann, 2010; Thompson et al., 2010) (HadSST3: 1965–1973: –0.63°C per decade, 1966–1974: –0.61°C per decade; ERSSTv5: 1965–1973: –0.60°C per decade, 1966–1974: –0.64°C per decade). Hereafter, we focus on the 1966-1974 trends in both datasets for simplicity of comparison. Both NH cooling and SH warming contribute comparable magnitudes to the 1966-1974 shift (**Table 3**). The most positive observational NH-SH trend is centered in 1922 (1918–1926) in both datasets, also with contributions from both hemispheres (**Table 3**).

Though the CMIP5 historical ensemble mean interhemispheric SST contrast has a negative trend in the 1960s and 1970s, the 1966–1974 trend magnitude is less than 10% of that in the observations (–0.051°C per decade), suggesting only a modest role of forcing in the observed trend. As shown in **Figure 5c**, the 1966–1974 observational trends are larger than any of the 36 historical realizations over this period. The 1918–1926 observational interhemispheric SST trends are also much larger than the CMIP5 historical ensemble mean (0.008°C per decade), but not as far outside the distribution of the 36 individual realizations as the 1970 shift (**Figure 5b**).

Accepted for publication in *Journal of Climate*. DOI 10.1175/JCLI-D-19-0102.1.

The observational spatial SST trends are shown for the two periods in **Figures 5d-5g**. The 1966–1974 trends (**Figures 5e** and **5g**) have a prominent north–south SST dipole pattern in the Atlantic, with pronounced cooling in the subpolar North Atlantic and warming in the extratropical South Atlantic, extending to the other mid-latitude basins. There is also strong cooling in the central equatorial and northeast Pacific, and a warming in the northwest Atlantic offshore the northeast US. The 1918–1926 trends (**Figures 5d** and **5f**) have pronounced cooling from 35°–50°S in the Atlantic and Indian sectors. There is strong warming in the equatorial Atlantic, Labrador Sea, the northeast Pacific, and the northern Nordic and Barents seas (where not masked in ERSSTv5). The spatial trend patterns are very similar if the historical multimodel mean SST is regressed out at each gridbox (not shown).

6.2 Forced and unforced contributions to the 1970 and 1920s shifts

We examine the contributions of forced and unforced variability to the 1970 and 1920s shifts, based on the detection and attribution best-estimate residuals from **Section 4**. **Figure 6a** shows $\hat{\varepsilon}_{obs}$ (from **Figure 3d**) and their 9-year running trends. The 1966–1974 shift remains the most prominent in both best-estimate residuals, corresponding to 87% and 77% of the respective magnitudes of the trends in HadSST3 and ERSSTv5 respectively (**Table 3**). The 1918–1926 interhemispheric trend remains nearly the same magnitude in the best-estimate residual HadSST3 as the full dataset (94% unforced), but is more reduced in ERSSTv5 (71% unforced).

We also examine the $\hat{\varepsilon}_{obs\_NH}$ (**Figure 6b**) and $\hat{\varepsilon}_{obs\_SH}$ (**Figure 6c**) contributions to the interhemispheric SST shifts. Both shifts result from additive trends of the NH and SH best-estimate residuals: NH cooling plus SH warming from 1966–1974; and NH warming plus SH cooling from 1918–1926. $\hat{\varepsilon}_{obs\_NH}$ has pronounced cooling trends over 1966-1974 (**Table 3**), with

Accepted for publication in *Journal of Climate*. DOI 10.1175/JCLI-D-19-0102.1.

the largest magnitude 9-year trend over the entire record for HadSST3, and the second-largest in ERSSTv5 after cooling around 1900; $\hat{\varepsilon}_{obs\_SH}$ also has large warming over this period in ERSSTv5. Warming in $\hat{\varepsilon}_{obs\_NH}$ and cooling in $\hat{\varepsilon}_{obs\_SH}$ also interfere constructively to produce the 1918–1926 interhemispheric SST trend.

Figure 7a compares the 1966–1974 trends in observations and best-estimate residuals $\hat{\varepsilon}_{obs}$ with the largest-magnitude negative (SH–NH) 9-year interhemispheric SST trends in each of the non-overlapping 132-year control segments. The 1966–1974 observed interhemispheric SST trends (solid lines) exceed all trends from the control simulations; however, the reduced-magnitude $\hat{\varepsilon}_{obs}$ trends (dashed lines) are comparable to some of the largest-magnitude control trends. The largest-magnitude negative segments are found in HadGEM2-ES, CSIRO-Mk3-6-0, IPSL-CM5A-LR, and GFDL-CM3, which are among the high-standard-deviation models in **Figure 3e**. [Several control segments exceed the 1918–1926 observational and $\hat{\varepsilon}_{obs}$ trend magnitudes (not shown)].

Figures 7b-7f show the spatial patterns associated with the 5 largest-magnitude negative interhemispheric SST trends in the control simulations indicated in **Figure 7a**. The trends have general agreement with an interhemispheric dipole in the in the tropical and subtropical Atlantic, with cooling in the NH and warming in the SH. HadGEM2-ES years 114–122 (**Figure 7d**) and GFDL-CM3 years 14–22 (**Figure 7f**) show strong subpolar Atlantic cooling with warming extending off the northeast US, and GFDL-CM3 years 14–22 also shows prominent subpolar SH warming in the Weddell Sea region. In contrast, IPSL-CM5A-LR years 608–616 has subpolar North Atlantic warming south of Greenland (**Figure 7c**). CSIRO-Mk3-6-0 years 310–318 (**Figure 7b)** and HadGEM2-ES years 364–372 (**Figure 7e**) have a horseshoe-pattern of mid-latitude cooling associated with North Atlantic SST variability (Gastineau and Frankignoul,

Accepted for publication in *Journal of Climate*. DOI 10.1175/JCLI-D-19-0102.1.

2015) but are less prominent in the central subpolar region. In the Pacific, CSIRO-Mk3-6-0 years 310–318 (**Fig. 7b**) shows a triangle-shaped pattern resembling the transition to the negative phase of the Pacific Decadal Oscillation (PDO) / Interdecadal Pacific Oscillation (IPO) (Zhang et al. 1997; Mantua et al. 1997; Power et al. 1999), with the other model episodes generally showing the opposite phase.

7. Summary and discussion

7.1 Summary

In this study, we quantify the variability of the interhemispheric SST contrast, motivated by its importance for tropical rainfall. We examine the variability of the 3-year mean interhemispheric SST contrast from 1881 to 2012 in the HadSST3 and ERSSTv5 datasets, applying a detection and attribution analysis using multimodel mean fingerprints from 36 total realizations of 10 CMIP5 models to identify the contributions from natural and anthropogenic forcing. We also investigate the constituent northern hemisphere (NH) and southern hemisphere (SH) SST variability. Our key findings include the following:

(a) The temporal magnitude of observed interhemispheric SST variability is within the range of the historical CMIP5 simulations examined. The observed spatial pattern of the interhemispheric SST contrast projects most strongly over the subpolar North Atlantic and the extratropical South Atlantic and Indian oceans. The historical model mean spatial pattern also has strong amplitudes over the extratropical South Atlantic and Indian oceans, but is much stronger over the North Pacific than the North Atlantic. The tropical rainbands shift toward the

Accepted for publication in *Journal of Climate*. DOI 10.1175/JCLI-D-19-0102.1.

relatively warmer SST hemisphere in both observations and models, though most models underestimate the precipitation response over northern tropical land regions.

(b) Anthropogenic, but not natural forcing, is detected at the 95% significance level in the interhemispheric SST contrast. The anthropogenic scaling factors are consistent with the multimodel mean in HadSST3, but results with ERSSTv5 suggest a larger interhemispheric SST response to forcing than simulated in the multimodel mean. We find a significantly larger amplitude of the anthropogenic influence on SH SST than the multimodel mean in both datasets. Natural forcing is detected (p<0.05) in the NH and SH in HadSST3 only.

(c) After removing the multimodel mean forced signal, the best-estimate residual unforced interhemispheric SST variability is largely consistent in magnitude with that of the control simulations and best-estimate residual historical simulations. However, the best-estimate residual individual NH and SH SST have relatively larger-magnitude variability and are more positively correlated than in any of the control simulations examined.

(d) Using 9-year running trends, we determine that the NH–SH interhemispheric decrease around 1970 is the most prominent shift over the instrumental period, corroborating previous identification (Baines and Folland, 2007; Dima and Lohmann, 2010; Thompson et al., 2010). Based on the multimodel mean detection and attribution analysis, we find that the shift was largely unforced, and due to both unforced NH cooling and SH warming. Interhemispheric SST shifts of comparable magnitude as the best-estimate residual 1970 shift are found in the control simulations of some of the high-variability models (CSIRO-Mk3-6-0, IPSL-CM5A-LR, HadGEM2-ES, and GFDL-CM3).

7.2 Discussion

Accepted for publication in *Journal of Climate*. DOI 10.1175/JCLI-D-19-0102.1.

Here, we consider some potential caveats and issues raised by our analysis. In the same way that the early 21st century global mean surface temperature slowdown motivated further research into the global energy balance and ocean heat content (Xie, 2016; Yan et al., 2016; Medhaug et al., 2017), we hope that examination of interhemispheric SST variability can underlie future mechanistic insights.

7.2.1 Fingerprint uncertainties

One caveat is that we do not consider inter-model differences in the multimodel mean fingerprints in our detection and attribution framework, which would add to the scaling factor uncertainties (Hannart et al., 2014; Schurer et al., 2018). First, there is inter-model spread in the GHG-only response, which may be due to non-CO_2 forcings as well as different feedbacks (Jones et al. 2016). **Figure 8a** shows the 3-year mean interhemispheric SST contrast anomaly time series in 35 historical GHG-only (historicalGHG) realizations (all historical realizations in **Table 1** except for IPSL-CM5A-MR). The multimodel mean time series has a positive 1881-2012 trend of 0.10±0.02 °C per 100 years (slope±2 adjusted standard errors, widened by a factor of $\sqrt{3}$ as described in **Section 3**). There are still considerable differences among the individual model mean trends, which provide an estimate of the range of the forced response: from –0.04±0.04 °C per 100 years in CSIRO-Mk3-6-0 to 0.31±0.05 °C per 100 years in IPSL-CM5A-LR (**Figure 8b**). [Model mean trends are calculated for the 7 models with more than 1 realization]. The spread of individual realizations is wider, from –0.21 to 0.38°C per 100 years, as it includes a larger contribution of model internal variability (with each realization combining forced and internal variability comparable to the actual climate). We compare the 1881-2012 historicalGHG interhemispheric SST trends with those of global mean SST (including gridpoints

Accepted for publication in *Journal of Climate*. DOI 10.1175/JCLI-D-19-0102.1.

from 5°S–5°N) for each realization in **Figure 8c**. The trends are strongly positively correlated (r=0.58), suggesting that the interhemispheric SST contrast scales with global mean SST in the GHG-forced response.

Anthropogenic aerosol forcing also remains a large uncertainty in the multimodel mean anthropogenic fingerprint. Though all models examined except bcc-csm1-1 do contain some representation of sulfate aerosol indirect effects, inter-model differences in aerosol parameterization result in different magnitudes and spatial patterns of aerosol forcing (Ekman, 2014; Guo et al., 2015; Allen et al., 2015; Rotstayn et al., 2015), particularly related to aerosol-cloud interactions (Chung and Soden, 2017). As only a subset of the CMIP5 modeling groups archived specific-forced historical anthropogenic-aerosol-only (historicalAA) realizations, we approximate the historicalAA interhemispheric contrast anomaly by subtracting the respective historicalGHG and historicalNat interhemispheric SST contrast time series from the historical interhemispheric SST contrast for each of the 35 realizations with historicalGHG output (**Figure 8d**). Note that the internal variability of the approximate historicalAA time series will typically be larger than for an individual experiment due to it being derived from multiple experiments (historical–historicalGHG–historicalNat), which contributes to some of the inter-model spread.

For a sense of the magnitude of the aerosol response, we examine the interhemispheric SST contrast during the mid-20th century period of maximum interhemispheric aerosol forcing (Rotstayn and Lohmann, 2002; Hwang et al., 2013; Wilcox et al., 2013), using the 1950-1985 trend as in Allen et al. (2015), shown in **Figure 8e**. The ensemble mean time series has a significant trend of –0.068±0.014 °C per decade (slope±2 adjusted standard errors), and the model mean trends range from –0.16±0.04 °C per decade in HadGEM2-ES to –0.012±0.032 °C per decade in CNRM-CM5. For comparison, the observed trends over this period are –0.11±0.05

Accepted for publication in *Journal of Climate*. DOI 10.1175/JCLI-D-19-0102.1.

and –0.16±0.039 °C per decade in HadSST3 and ERSSTv5 respectively. Improvements in spatiotemporal aerosol emission patterns and better treatment of aerosol probabilities may reduce some of the uncertainties (Schurer et al., 2018; Haustein et al., 2019). Another partially-anthropogenic influence on the interhemispheric SST contrast is African dust emissions from land use change, which are poorly simulated by CMIP5 models (Evan et al., 2014; Allen et al., 2015).

Detection of natural forcing in the HadSST3 (which not being infilled is generally preferred for attribution) individual hemispheres, yet not the interhemispheric SST contrast, suggests that natural forcing over the 20th century does not show a pronounced enough hemispheric SST contrast to be detectible, despite some hemispheric asymmetry in volcanic forcing (Haywood et al., 2013; Iles and Hegerl, 2014). Recent studies increasingly show a volcanic influence on large-scale climate modes, including the AMOC, but the responses may not be well-represented across models due to their complex lagged processes and limited eruption observations over the historical period (Swingedouw et al., 2017). For instance, the 1963 Agung eruption may have forced part of the North Atlantic cooling that contributed to the interhemispheric shift around 1970 (Swingedouw et al., 2013; Hodson et al., 2014). Some observational analyses also suggest that solar variability may modulate the interhemispheric SST contrast (Rajesh and Tiwari, 2018), though detection and attribution studies have so far not found a significant solar influence on large-scale surface temperatures (Schurer et al. 2014).

7.2.2 Spatial and basin interhemispheric SST variability

While the basic time series diagnostics (**Figures 1c-1d)** suggest that the CMIP5 models effectively reproduce the temporal characteristics of the interhemispheric SST contrast,

Accepted for publication in *Journal of Climate*. DOI 10.1175/JCLI-D-19-0102.1.

comparison of the observed (**Figures 2a** and **2c**) and model mean (**Figure 2e**) spatial patterns points to some differences in the mechanisms involved. In particular, the model-mean spatial pattern has much stronger positive slopes over the North Pacific, whereas the observations have the most pronounced positive amplitudes over the subpolar North Atlantic. However, we note that the relatively short observational record and uneven SST observational data distribution, with much more data from the North Atlantic, makes it difficult to evaluate the significance of these spatial pattern differences.

Examination of intra-model interhemispheric SST pattern variability suggests that the extratropical North Atlantic may be more important than suggested by the multimodel mean pattern. **Figure 9** shows the ensemble standard deviation of the 36 CMIP5 historical SST regression slopes averaged in **Figure 2e**. The large inter-model variability over the extratropical North Atlantic north of 40°N contrasts with the weak model-mean slopes in this region in **Figure 2e**, suggesting that the different patterns cancel out in the multimodel mean.

There are similar questions about the importance of different ocean basins in the large-magnitude interhemispheric SST shifts. The spatial patterns of the 1920s and 1970 interhemispheric SST shifts (**Figures 5d**-**5g)** could result from linked ocean basin SST variability, as proposed between Atlantic and Pacific SST (Zhang and Delworth 2007; Chafik et al. 2016). On the other hand, the different ocean basins may be independent, as Goosse (2017) cautions that interhemispheric SST shifts can result from the superposition of unrelated processes. Among the control shifts, the sign difference in the eastern Pacific in CSIRO-Mk3-6-0 years 310–318 suggests different representations linking Pacific and Atlantic SST variability, or possibly that that IPO-related Pacific variability is not important for the interhemispheric SST contrast as it extends into both hemispheres. The eastern Pacific is much less prominent in the

Accepted for publication in *Journal of Climate*. DOI 10.1175/JCLI-D-19-0102.1.

observed shifts than in the large-magnitude control shifts, though the 1970 shift does show strong central and northeast Pacific SST cooling extending to southwest North America.

Next, we discuss the subpolar North Atlantic and potential AMOC contribution to interhemispheric SST shifts. The mechanism of cross-equator ocean heat transport via the AMOC is thought to explain the interhemispheric "bipolar seesaw" SST pattern in glacial-interglacial paleoclimate records (Crowley, 1992; Broecker, 1998) and has been found in many modeling experiments (Vellinga and Wu, 2004; Latif et al., 2006; Stouffer et al., 2007; Sun et al., 2013, 2018). Some studies have thus used the interhemispheric SST contrast as a proxy for the AMOC (e.g. Dima and Lohmann, 2010), though the Atlantic interhemispheric SST pattern has been found to be a weaker AMOC indicator than North Atlantic SST in most CMIP5 models (Muir and Fedorov, 2015)

An observational limitation is that continuous direct measurements of the AMOC only began in 2004 (with altimetry extending the record to 1993), which is not nearly long enough to resolve decadal and multidecadal variability. Recently, it has been proposed that the century-long SST cooling trend in the subpolar North Atlantic, sometimes referred to as the "warming hole", indicates a long-term decrease in the AMOC over the 20th century (Drijfhout et al., 2012; Rahmstorf et al., 2015; Caesar et al., 2018), though the relationship between these surface changes and the AMOC remains contested (Josey et al., 2018). Negative trends in subpolar Atlantic surface salinity and density since the early 20th century are consistent with an AMOC decrease, though other factors could also be responsible (Friedman et al., 2017; Reverdin et al., 2019). Oceanographic proxy reconstructions also suggest a longer-term AMOC decline since the end of the Little Ice Age (Thibodeau et al., 2018; Thornalley et al., 2018).

Accepted for publication in *Journal of Climate*. DOI 10.1175/JCLI-D-19-0102.1.

As an indirect index of the AMOC, we calculate an AMOC proxy SST time series following Rahmstorf et al. (2015) and Caesar et al. (2018) as the difference of the North Atlantic subpolar gyre (SPG; 50°–15°W, 50°–60°N) and global mean SST, using 3-year running annual means and masked as shown in **Figure 1b**. First, we briefly examine the long-term GHG-forced trends of the AMOC proxy SST index. The 1881–2012 historicalGHG multimodel mean trend of the AMOC proxy SST index (of the models examined in **Figures 8a-8c**) is –0.50±0.07 °C per 100 years (slope±2 adjusted standard errors), consistent with the GHG-forced AMOC slowdown simulated by the models (Caesar et al., 2018). We find that the 1881–2012 AMOC proxy SST index trends are very strongly correlated with the respective interhemispheric SST trends across the historicalGHG simulations (r=0.77).

Next, we examine the observed and historical SST AMOC proxy time series variability. **Figure 10a** shows the observed interhemispheric SST contrast and 3-year mean SST AMOC proxy time series anomalies. Though they are strongly correlated (HadSST3: r=0.63; ERSSTv5: r=0.58), the AMOC proxy SST time series shows stronger variability on longer decadal timescales, and the interhemispheric SST contrast lacks the long-term 20th century trend in the AMOC proxy SST time series. **Figure 10b** compares the observed correlations of the interhemispheric SST contrast and the AMOC SST proxy index with the historical models. The observed correlations are stronger than nearly all of the historical realizations, with some models showing zero or negative correlations. This is consistent with the discrepancy between **Figure 2e** and **Figures 2a** and **2c,** indicating that the Atlantic SPG plays a much larger role in the observed interhemispheric SST contrast than in most models. This suggests that many models could be misrepresenting some processes of Atlantic interhemispheric SST variability related to the AMOC, or a common response to forcings.

Accepted for publication in *Journal of Climate*. DOI 10.1175/JCLI-D-19-0102.1.

Looking forward, simulation of Atlantic interhemispheric SST variability may improve with increasing model resolution. For example, Hutchinson et al. (2015) find a larger interhemispheric temperature response in an Atlantic-sector coupled climate model using an eddy-permitting 0.25° ocean resolution compared to a 1° resolution which is typical of CMIP5 models. North Atlantic decadal variability may also improve with correction of North Atlantic mean state biases, particularly salinity, related to AMOC variability (Menary et al., 2015; Park et al., 2016; Liu et al., 2017).

A related question is the role of the AMOC in the interhemispheric SST shifts in the 1920s and around 1970. The AMOC proxy SST time series of **Figure 10a** shows a rapid drop during the 1970 shift, though not as prominent in the overall record given the larger decadal variability. The spatial SST pattern associated with the 1970 shift (**Figures 5e** and **5g**) shows an Atlantic interhemispheric SST dipole suggested as an AMOC fingerprint (e.g. (Dima and Lohmann, 2010)) as well as the specific AMOC slowdown pattern of subpolar Atlantic cooling and warming offshore the northeast United States (Saba et al., 2016; Caesar et al., 2018). Subsurface salinity and temperature profiles also suggest an AMOC decline during the mid-20th century concurrent with the interhemispheric SST shift around 1970 (Hodson et al., 2014). However, determining the role of the AMOC from alternative mechanisms is difficult on such short timescales given the lack of data over the period. For example, Wang et al. (2015) showed that atmospheric teleconnections can also produce an interhemispheric Atlantic SST dipole pattern. In contrast, the 1920s do not have a persistent increase in the AMOC proxy SST record in **Figure 10a**, but rather strong inter-annual variability. Likewise, the spatial SST pattern associated with the 1920s shift (**Figures 5d** and **5f**) does not have an Atlantic interhemispheric dipole; the sign change is around 30°S rather than in the equatorial Atlantic.

Accepted for publication in *Journal of Climate*. DOI 10.1175/JCLI-D-19-0102.1.

Decadal shifts in the subpolar North Atlantic have previously been described in several different unforced simulations involving linkages between blocking, sea ice, and AMOC feedbacks (Drijfhout et al., 2013; Kleppin et al., 2015; Moreno-Chamarro et al., 2015; Sgubin et al., 2017). Understanding how these different processes may contribute to the interhemispheric SST shifts in the control simulations remains a topic of future investigation. Among our sample of large-magnitude events (**Figure 7b**–**7e**), HadGEM2-ES years 114-122 and GFDL-CM3 years 14–22 show strong and coherent cooling in the subpolar North Atlantic and warming in the Gulf Stream extension, which are consistent with the spatial fingerprint of an AMOC slowdown (Saba et al., 2016; Caesar et al., 2018); GFDL-CM3 in particular has been found to have large-amplitude multidecadal AMOC variability (Cheng et al., 2013). The warming found in GFDL-CM3 years 14–22 in the high-latitude SH adjacent to Antarctica has been suggested to be an AMOC slowdown signature (Dima and Lohmann, 2010). Though the IPSL-CM5A-LR control shift in years 608–616 shows strong *warming* in the subpolar North Atlantic, this could potentially be due to the AMOC: as shown in Muir and Fedorov (2015) (their Figure 4), the IPSL-CM5A-LR AMOC SST spatial pattern has anomalies of opposing sign in the subpolar North Atlantic.

7.2.3 NH and SH variability

An intriguing finding from our detection and attribution analysis is that the best-estimate residual NH and SST are more positively correlated than in any of the control simulations (**Figure 4h**). Likewise, the best-estimate residual NH and SH SST standard deviations are at the upper end of the control simulation variability (**Figure 4g**), which is not the case for the interhemispheric SST contrast (**Figure 3e**). The positive best-estimate residual NH and SH SST

Accepted for publication in *Journal of Climate*. DOI 10.1175/JCLI-D-19-0102.1.

correlation and large-magnitude variability are consistent: the in-phase residual NH and SH SST variations have a canceling influence on the interhemispheric SST contrast.

There are a couple of possibilities that could account for the large positive best-estimate residual NH and SH SST correlation and large-magnitude variability. One explanation, related to the fingerprint uncertainties discussed in **Section 7.2.1**, is that there is a common NH and SH forced component which is missing or underestimated by the models. For example, climate models may underestimate the cooling from early 20th century eruptions, such as 1912 Katmai (1912) and Colima (1913), accounting for the early 20th century discrepancies between the NH and SH fingerprints and observations in **Figures 4a-4b.**

Common SST data biases in the NH and SH could also artificially inflate the correlation. Recent studies examining geographic biases (Cowtan et al. 2018; Chan and Huybers 2019) and hemispheric and global time series (Folland et al., 2018; Haustein et al., 2019) have found that WWII-era warming and potentially also some cooling around 1900 remain inflated in gridded observational data products. A third possibility is that the models may underestimate common decadal variability in the NH and SH SST. IPO-related Pacific decadal variability, which has been linked to excursions in global mean surface temperature (Kosaka and Xie, 2013; Maher et al., 2014; England et al., 2014; Dai et al., 2015; Gastineau et al., 2019), is underestimated by many CMIP5 models (Kociuba and Power, 2015; Henley et al., 2017). Pacific decadal variability may account for some of the joint negative values in residual NH and SH SST after around 2000 (**Figures 4e-4f**), reflecting lower global mean SST than the CMIP5 historical model mean in the so-called *hiatus* or slowdown (Fyfe et al. 2013; Medhaug et al. 2017).

These discrepancies raise questions about the use of model control experiments to simulate background variability, as in many detection and attribution studies (as well as other analyses

Accepted for publication in *Journal of Climate*. DOI 10.1175/JCLI-D-19-0102.1.

such as future projections). Using control simulations with unrealistic variability means that the confidence intervals calculated in analyses using them may be over- or under-confident, which could lead to misleading conclusions. In the future, perhaps the simulation of internal variability should be treated more explicitly in model selection (e.g. Knutti et al., 2010).

Acknowledgments

A.R.F, G.C.H., and A.S. were supported by the ERC-funded TITAN project (EC-320691). A.R.F. was also supported by the U.S. NSF grant EAPSI-1311103 and the UK NERC-funded SMURPHs project (NE/N006143/1). G.C.H. and A.S. were further supported by the UK NERC under the Belmont forum, Grant PacMedy (NE/P006752/1). S.-Y.L. was funded by the Taiwan NSC grant 102-2611-M-001-006. J.C.H.C was supported by the U.S. DOE Office of Science, Biological and Environmental Research program (DE-FG02-08ER64588). The HadSST3 data were provided by the UK Met Office Hadley Center, and the ERSSTv5 data were provided by the U.S. NOAA's National Centers for Environmental Information. We acknowledge the World Climate Research Program's Working Group on Coupled Modeling, which is responsible for CMIP and the climate modeling groups for producing and making available their model output. For CMIP the U.S. DOE's Program for Climate Model Diagnosis and Intercomparison provides coordinating support and led development of software infrastructure in partnership with the Global Organization for Earth System Science Portals. The CMIP5 output was hosted by the UK Center for Environmental Data Analysis. We thank Debbie Polson for providing the detection and attribution code and Mike Mineter for valuable assistance. We appreciate the constructive feedback from three anonymous reviewers.

Accepted for publication in *Journal of Climate*. DOI 10.1175/JCLI-D-19-0102.1.

Appendix: historical simulation residuals

The best-estimate residuals are estimated for each historical realization as follows. Building on Schurer et al. (2015), we modify the denominator scaling in **Equation (4)** to account for the component of shared variance of each individual historical realization time series with the model mean fingerprint $X_{historical}$ (the average of all historical realization time series):

$$\hat{\varepsilon}_{historical} = \frac{(\gamma_{historical} - \beta_1 X_{historicalNat} - \beta_2 X_{historical})}{\sqrt{\frac{\beta_1^2}{n} + \frac{(n-\beta_2)^2 + \beta_2^2(n-1)}{n^2}}} \quad , \qquad \text{(A1)}$$

where $\gamma_{historical}$ is the respective historical realization time series.

Accepted for publication in *Journal of Climate*. DOI 10.1175/JCLI-D-19-0102.1.

References

Allen, M.R., Stott, P.A., 2003. Estimating signal amplitudes in optimal fingerprinting, part I: theory. Clim. Dyn. 21, 477–491. https://doi.org/10.1007/s00382-003-0313-9

Allen, R.J., Evan, A.T., Booth, B.B.B., 2015. Interhemispheric Aerosol Radiative Forcing and Tropical Precipitation Shifts during the Late Twentieth Century. J. Clim. 28, 8219–8246. https://doi.org/10.1175/JCLI-D-15-0148.1

Armour, K.C., Marshall, J., Scott, J.R., Donohoe, A., Newsom, E.R., 2016. Southern Ocean warming delayed by circumpolar upwelling and equatorward transport. Nat. Geosci. 9, 549–554. https://doi.org/10.1038/ngeo2731

Baines, P., Folland, C., 2007. Evidence for a rapid global climate shift across the late 1960s. J. Clim. 20, 2721–2744. https://doi.org/10.1175/JCLI4177.1

Becker, A., Finger, P., Meyer-Christoffer, A., Rudolf, B., Schamm, K., Schneider, U., Ziese, M., 2013. A description of the global land-surface precipitation data products of the Global Precipitation Climatology Centre with sample applications including centennial (trend) analysis from 1901–present. Earth Syst. Sci. Data 5, 71–99. https://doi.org/10.5194/essd-5-71-2013

Biasutti, M., Held, I.M., Sobel, A.H., Giannini, A., 2008. SST Forcings and Sahel Rainfall Variability in Simulations of the Twentieth and Twenty-First Centuries. J. Clim. 21, 3471–3486.

Bindoff, N.L., Stott, P.A., AchutaRao, K.M., Allen, M.R., Gillett, N., Gutzler, D., Hansingo, K., Hegerl, G., Hu, Y., Jain, S., Mokhov, I.I., Overland, J., Perlwitz, J., Sebbari, R., Zhang, X., 2013. Detection and Attribution of Climate Change: from Global to Regional, in: Climate Change 2013: The Physical Science Basis. Contribution of Working Group I to the Fifth Assessment Report of the Intergovernmental Panel on Climate Change. Cambridge University Press, Cambridge, pp. 867–952.

Bond, T.C., Doherty, S.J., Fahey, D.W., Forster, P.M., Berntsen, T., DeAngelo, B.J., Flanner, M.G., Ghan, S., Kärcher, B., Koch, D., Kinne, S., Kondo, Y., Quinn, P.K., Sarofim, M.C., Schultz, M.G., Schulz, M., Venkataraman, C., Zhang, H., Zhang, S., Bellouin, N., Guttikunda, S.K., Hopke, P.K., Jacobson, M.Z., Kaiser, J.W., Klimont, Z., Lohmann, U., Schwarz, J.P., Shindell, D., Storelvmo, T., Warren, S.G., Zender, C.S., 2013. Bounding the role of black carbon in the climate system: A scientific assessment. J. Geophys. Res. Atmospheres 118, 5380–5552. https://doi.org/10.1002/jgrd.50171

Booth, B.B.B., Harris, G.R., Jones, A., Wilcox, L., Hawcroft, M., Carslaw, K.S., 2018. Comments on "Rethinking the Lower Bound on Aerosol Radiative Forcing." J. Clim. 31, 9407–9412. https://doi.org/10.1175/JCLI-D-17-0369.1

Boucher, O., Randall, D., Artaxo, P., Bretherton, C., Feingold, G., Forster, P., Kerminen, V.-M., Kondo, Y., Liao, H., Lohmann, U., 2013. Clouds and aerosols, in: Climate Change 2013: The Physical Science Basis. Contribution of Working Group I to the Fifth Assessment Report of the Intergovernmental Panel on Climate Change. Cambridge University Press, pp. 571–657.

Broecker, W.S., 1998. Paleocean circulation during the Last Deglaciation: A bipolar seesaw? Paleoceanography 13, 119–121. https://doi.org/10.1029/97PA03707

Caesar, L., Rahmstorf, S., Robinson, A., Feulner, G., Saba, V., 2018. Observed fingerprint of a weakening Atlantic Ocean overturning circulation. Nature 556, 191–196. https://doi.org/10.1038/s41586-018-0006-5

Accepted for publication in *Journal of Climate*. DOI 10.1175/JCLI-D-19-0102.1.

749 Chafik, L., Häkkinen, S., England, M.H., Carton, J.A., Nigam, S., Ruiz-Barradas, A., Hannachi, A.,
750 Miller, L., 2016. Global linkages originating from decadal oceanic variability in the
751 subpolar North Atlantic. Geophys. Res. Lett. 43, 2016GL071134.
752 https://doi.org/10.1002/2016GL071134
753 Chan, D., Huybers, P., 2019. Systematic Differences in Bucket Sea Surface Temperature
754 Measurements among Nations Identified Using a Linear-Mixed-Effect Method. J.
755 Clim. 32, 2569–2589. https://doi.org/10.1175/JCLI-D-18-0562.1
756 Chang, C.-Y., Chiang, J.C.H., Wehner, M.F., Friedman, A.R., Ruedy, R., 2011. Sulfate aerosol
757 control of Tropical Atlantic climate over the Twentieth Century. J. Clim.
758 110301125651015. https://doi.org/10.1175/2010JCLI4065.1
759 Cheng, W., Chiang, J.C.H., Zhang, D., 2013. Atlantic Meridional Overturning Circulation
760 (AMOC) in CMIP5 Models: RCP and Historical Simulations. J. Clim. 26, 7187–7197.
761 https://doi.org/10.1175/JCLI-D-12-00496.1
762 Chiang, J.C.H., Friedman, A.R., 2012. Extratropical Cooling, Interhemispheric Thermal
763 Gradients, and Tropical Climate Change. Annu. Rev. Earth Planet. Sci. 40, 383–412.
764 https://doi.org/10.1146/annurev-earth-042711-105545
765 Chung, C., Ramanathan, V., 2007. Relationship between trends in land precipitation and
766 tropical SST gradient. Geophys. Res. Lett. 34.
767 https://doi.org/10.1029/2007GL030491
768 Chung, E.-S., Soden, B.J., 2017. Hemispheric climate shifts driven by anthropogenic aerosol–
769 cloud interactions. Nat. Geosci. 10, 566–571. https://doi.org/10.1038/ngeo2988
770 Cowtan, K., Rohde, R., Hausfather, Z., 2018. Evaluating biases in sea surface temperature
771 records using coastal weather stations. Q. J. R. Meteorol. Soc. 144, 670–681.
772 https://doi.org/10.1002/qj.3235
773 Crowley, T.J., 1992. North Atlantic Deep Water cools the southern hemisphere.
774 Paleoceanography 7, 489–497. https://doi.org/10.1029/92PA01058
775 Dai, A., 2013. The influence of the inter-decadal Pacific oscillation on US precipitation
776 during 1923–2010. Clim. Dyn. 41, 633–646. https://doi.org/10.1007/s00382-012-
777 1446-5
778 Dai, A., Fyfe, J.C., Xie, S.-P., Dai, X., 2015. Decadal modulation of global surface temperature
779 by internal climate variability. Nat. Clim. Change 5, 555–559.
780 https://doi.org/10.1038/nclimate2605
781 Dickson, R.R., Meincke, J., Malmberg, S.-A., Lee, A.J., 1988. The “great salinity anomaly” in
782 the northern North Atlantic 1968–1982. Prog. Oceanogr. 20, 103–151.
783 Dima, M., Lohmann, G., 2010. Evidence for Two Distinct Modes of Large-Scale Ocean
784 Circulation Changes over the Last Century. J. Clim. 23, 5–16.
785 https://doi.org/10.1175/2009JCLI2867.1
786 Drijfhout, S., Gleeson, E., Dijkstra, H.A., Livina, V., 2013. Spontaneous abrupt climate change
787 due to an atmospheric blocking–sea-ice–ocean feedback in an unforced climate
788 model simulation. Proc. Natl. Acad. Sci. 110, 19713–19718.
789 https://doi.org/10.1073/pnas.1304912110
790 Drijfhout, S., van Oldenborgh, G.J., Cimatoribus, A., 2012. Is a Decline of AMOC Causing the
791 Warming Hole above the North Atlantic in Observed and Modeled Warming
792 Patterns? J. Clim. 25, 8373–8379. https://doi.org/10.1175/JCLI-D-12-00490.1

Accepted for publication in *Journal of Climate*. DOI 10.1175/JCLI-D-19-0102.1.

793 Drost, F., Karoly, D., 2012. Evaluating global climate responses to different forcings using
794 simple indices. Geophys. Res. Lett. 39, L16701.
795 https://doi.org/10.1029/2012GL052667
796 Ekman, A.M.L., 2014. Do sophisticated parameterizations of aerosol-cloud interactions in
797 CMIP5 models improve the representation of recent observed temperature trends?
798 J. Geophys. Res. Atmospheres 119, 817–832.
799 https://doi.org/10.1002/2013JD020511
800 England, M.H., McGregor, S., Spence, P., Meehl, G.A., Timmermann, A., Cai, W., Gupta, A.S.,
801 McPhaden, M.J., Purich, A., Santoso, A., 2014. Recent intensification of wind-driven
802 circulation in the Pacific and the ongoing warming hiatus. Nat. Clim. Change 4, 222–
803 227. https://doi.org/10.1038/nclimate2106
804 Evan, A.T., Flamant, C., Fiedler, S., Doherty, O., 2014. An analysis of aeolian dust in climate
805 models. Geophys. Res. Lett. 41, 5996–6001.
806 https://doi.org/10.1002/2014GL060545
807 Feulner, G., Rahmstorf, S., Levermann, A., Volkwardt, S., 2013. On the Origin of the Surface
808 Air Temperature Difference between the Hemispheres in Earth's Present-Day
809 Climate. J. Clim. 26, 7136–7150. https://doi.org/10.1175/JCLI-D-12-00636.1
810 Folland, C., Palmer, T., Parker, D., 1986. Sahel Rainfall And Worldwide Sea Temperatures,
811 1901-85. Nature 320, 602–607.
812 Folland, C.K., Boucher, O., Colman, A., Parker, D.E., 2018. Causes of irregularities in trends of
813 global mean surface temperature since the late 19th century. Sci. Adv. 4, eaao5297.
814 https://doi.org/10.1126/sciadv.aao5297
815 Friedman, A.R., Hwang, Y.-T., Chiang, J.C.H., Frierson, D.M.W., 2013. Interhemispheric
816 Temperature Asymmetry over the Twentieth Century and in Future Projections. J.
817 Clim. 26, 5419–5433. https://doi.org/10.1175/JCLI-D-12-00525.1
818 Friedman, A.R., Reverdin, G., Khodri, M., Gastineau, G., 2017. A new record of Atlantic sea
819 surface salinity from 1896 to 2013 reveals the signatures of climate variability and
820 long-term trends. Geophys. Res. Lett. 2017GL072582.
821 https://doi.org/10.1002/2017GL072582
822 Fyfe, J.C., Gillett, N.P., Zwiers, F.W., 2013. Overestimated global warming over the past 20
823 years. Nat. Clim. Change 3, 767–769. https://doi.org/10.1038/nclimate1972
824 Gastineau, G., Frankignoul, C., 2015. Influence of the North Atlantic SST Variability on the
825 Atmospheric Circulation during the Twentieth Century. J. Clim. 28, 1396–1416.
826 https://doi.org/10.1175/JCLI-D-14-00424.1
827 Gastineau, G., Friedman, A.R., Khodri, M., Vialard, J., 2019. Global ocean heat content
828 redistribution during the 1998–2012 Interdecadal Pacific Oscillation negative
829 phase. Clim. Dyn. 53, 1187–1208. https://doi.org/10.1007/s00382-018-4387-9
830 Genovese, C.R., Lazar, N.A., Nichols, T., 2002. Thresholding of Statistical Maps in Functional
831 Neuroimaging Using the False Discovery Rate. NeuroImage 15, 870–878.
832 https://doi.org/10.1006/nimg.2001.1037
833 Goosse, H., 2017. Reconstructed and simulated temperature asymmetry between
834 continents in both hemispheres over the last centuries. Clim. Dyn. 48, 1483–1501.
835 https://doi.org/10.1007/s00382-016-3154-z
836 Guo, L., Turner, A.G., Highwood, E.J., 2015. Impacts of 20th century aerosol emissions on the
837 South Asian monsoon in the CMIP5 models. Atmospheric Chem. Phys. 15, 6367–
838 6378. https://doi.org/10.5194/acp-15-6367-2015

Accepted for publication in *Journal of Climate*. DOI 10.1175/JCLI-D-19-0102.1.

839 Hannart, A., Ribes, A., Naveau, P., 2014. Optimal fingerprinting under multiple sources of
840 uncertainty. Geophys. Res. Lett. 41, 1261–1268.
841 https://doi.org/10.1002/2013GL058653
842 Hansen, J., Ruedy, R., Sato, M., Lo, K., 2010. Global Surface Temperature Change. Rev.
843 Geophys. 48, 29 PP. https://doi.org/201010.1029/2010RG000345
844 Haustein, K., Otto, F.E.L., Venema, V., Jacobs, P., Cowtan, K., Hausfather, Z., Way, R.G., White,
845 B., Subramanian, A., Schurer, A.P., 2019. A Limited Role for Unforced Internal
846 Variability in Twentieth-Century Warming. J. Clim. 32, 4893–4917.
847 https://doi.org/10.1175/JCLI-D-18-0555.1
848 Haywood, J.M., Jones, A., Bellouin, N., Stephenson, D., 2013. Asymmetric forcing from
849 stratospheric aerosols impacts Sahelian rainfall. Nat. Clim. Change 3, 660–665.
850 https://doi.org/10.1038/nclimate1857
851 Hegerl, G., Zwiers, F., 2011. Use of models in detection and attribution of climate change.
852 Wiley Interdiscip. Rev. Clim. Change 2, 570–591. https://doi.org/10.1002/wcc.121
853 Hegerl, G.C., Black, E., Allan, R.P., Ingram, W.J., Polson, D., Trenberth, K.E., Chadwick, R.S.,
854 Arkin, P.A., Sarojini, B.B., Becker, A., Dai, A., Durack, P.J., Easterling, D., Fowler, H.J.,
855 Kendon, E.J., Huffman, G.J., Liu, C., Marsh, R., New, M., Osborn, T.J., Skliris, N., Stott,
856 P.A., Vidale, P.-L., Wijffels, S.E., Wilcox, L.J., Willett, K.M., Zhang, X., 2015. Challenges
857 in Quantifying Changes in the Global Water Cycle. Bull. Am. Meteorol. Soc. 96, 1097–
858 1115. https://doi.org/10.1175/BAMS-D-13-00212.1
859 Hegerl, G.C., Brönnimann, S., Schurer, A., Cowan, T., 2018. The early 20th century warming:
860 Anomalies, causes, and consequences. Wiley Interdiscip. Rev. Clim. Change 9, e522.
861 https://doi.org/10.1002/wcc.522
862 Hegerl, G.C., Hasselmann, K., Cubasch, U., Mitchell, J.F.B., Roeckner, E., Voss, R., Waszkewitz,
863 J., 1997. Multi-fingerprint detection and attribution analysis of greenhouse gas,
864 greenhouse gas-plus-aerosol and solar forced climate change. Clim. Dyn. 13, 613–
865 634. https://doi.org/10.1007/s003820050186
866 Henley, B.J., Meehl, G., Power, S.B., Folland, C.K., King, A.D., Brown, J.N., Karoly, D.J., Delage,
867 F., Gallant, A.J.E., Freund, M., Neukom, R., 2017. Spatial and temporal agreement in
868 climate model simulations of the Interdecadal Pacific Oscillation. Environ. Res. Lett.
869 12, 044011. https://doi.org/10.1088/1748-9326/aa5cc8
870 Hodson, D.L.R., Robson, J.I., Sutton, R.T., 2014. An Anatomy of the Cooling of the North
871 Atlantic Ocean in the 1960s and 1970s. J. Clim. 27, 8229–8243.
872 https://doi.org/10.1175/JCLI-D-14-00301.1
873 Hoesly, R.M., Smith, S.J., Feng, L., Klimont, Z., Janssens-Maenhout, G., Pitkanen, T., Seibert,
874 J.J., Vu, L., Andres, R.J., Bolt, R.M., Bond, T.C., Dawidowski, L., Kholod, N., Kurokawa, J.,
875 Li, M., Liu, L., Lu, Z., Moura, M.C.P., O'Rourke, P.R., Zhang, Q., 2018. Historical (1750–
876 2014) anthropogenic emissions of reactive gases and aerosols from the Community
877 Emissions Data System (CEDS). Geosci. Model Dev. 11, 369–408.
878 https://doi.org/10.5194/gmd-11-369-2018
879 Huang, B., Thorne, P.W., Banzon, V.F., Boyer, T., Chepurin, G., Lawrimore, J.H., Menne, M.J.,
880 Smith, T.M., Vose, R.S., Zhang, H.-M., 2017. Extended Reconstructed Sea Surface
881 Temperature, Version 5 (ERSSTv5): Upgrades, Validations, and Intercomparisons. J.
882 Clim. 30, 8179–8205. https://doi.org/10.1175/JCLI-D-16-0836.1

Accepted for publication in *Journal of Climate*. DOI 10.1175/JCLI-D-19-0102.1.

Hutchinson, D.K., England, M.H., M. Hogg, A., Snow, K., 2015. Interhemispheric Asymmetry of Warming in an Eddy-Permitting Coupled Sector Model. J. Clim. 28, 7385–7406. https://doi.org/10.1175/JCLI-D-15-0014.1

Hutchinson, D.K., England, M.H., Santoso, A., Hogg, A.McC., 2013. Interhemispheric asymmetry in transient global warming: The role of Drake Passage. Geophys. Res. Lett. 40, 1587–1593. https://doi.org/10.1002/grl.50341

Hwang, Y.-T., Frierson, D.M.W., Kang, S.M., 2013. Anthropogenic sulfate aerosol and the southward shift of tropical precipitation in the late 20th century. Geophys. Res. Lett. 40, 2845–2850. https://doi.org/10.1002/grl.50502

Iles, C.E., Hegerl, G.C., 2014. The global precipitation response to volcanic eruptions in the CMIP5 models. Environ. Res. Lett. 9. https://doi.org/10.1088/1748-9326/9/10/104012

Jones, G.S., Stott, P.A., Mitchell, J.F.B., 2016. Uncertainties in the attribution of greenhouse gas warming and implications for climate prediction. J. Geophys. Res. Atmospheres 121, 6969–6992. https://doi.org/10.1002/2015JD024337

Josey, S.A., Hirschi, J.J.-M., Sinha, B., Duchez, A., Grist, J.P., Marsh, R., 2018. The Recent Atlantic Cold Anomaly: Causes, Consequences, and Related Phenomena. Annu. Rev. Mar. Sci. 10, 475–501. https://doi.org/10.1146/annurev-marine-121916-063102

Kang, S.M., Seager, R., Frierson, D.M.W., Liu, X., 2014. Croll revisited: Why is the northern hemisphere warmer than the southern hemisphere? Clim. Dyn. 44, 1457–1472. https://doi.org/10.1007/s00382-014-2147-z

Kennedy, J.J., 2014. A review of uncertainty in in situ measurements and data sets of sea surface temperature. Rev. Geophys. 52, 1–32. https://doi.org/10.1002/2013RG000434

Kennedy, J.J., Rayner, N.A., Smith, R.O., Parker, D.E., Saunby, M., 2011a. Reassessing biases and other uncertainties in sea surface temperature observations measured in situ since 1850: 1. Measurement and sampling uncertainties. J. Geophys. Res. 116, 13 PP. https://doi.org/201110.1029/2010JD015218

Kennedy, J.J., Rayner, N.A., Smith, R.O., Parker, D.E., Saunby, M., 2011b. Reassessing biases and other uncertainties in sea surface temperature observations measured in situ since 1850: 2. Biases and homogenization. J. Geophys. Res. 116, 22 PP. https://doi.org/201110.1029/2010JD015220

Kiehl, J.T., Briegleb, B.P., 1993. The Relative Roles Of Sulfate Aerosols And Greenhouse Gases In Climate Forcing. Science 260, 311–314.

Kleppin, H., Jochum, M., Otto-Bliesner, B., Shields, C.A., Yeager, S., 2015. Stochastic Atmospheric Forcing as a Cause of Greenland Climate Transitions. J. Clim. 28, 7741–7763. https://doi.org/10.1175/JCLI-D-14-00728.1

Knutti, R., Furrer, R., Tebaldi, C., Cermak, J., Meehl, G.A., 2010. Challenges in Combining Projections from Multiple Climate Models. J. Clim. 23, 2739–2758. https://doi.org/10.1175/2009JCLI3361.1

Kociuba, G., Power, S.B., 2015. Inability of CMIP5 Models to Simulate Recent Strengthening of the Walker Circulation: Implications for Projections. J. Clim. 28, 20–35. https://doi.org/10.1175/JCLI-D-13-00752.1

Kosaka, Y., Xie, S.-P., 2013. Recent global-warming hiatus tied to equatorial Pacific surface cooling. Nature 501, 403–407. https://doi.org/10.1038/nature12534

Accepted for publication in *Journal of Climate*. DOI 10.1175/JCLI-D-19-0102.1.

928 Kretzschmar, J., Salzmann, M., Mülmenstädt, J., Boucher, O., Quaas, J., 2017. Comment on
929 "Rethinking the Lower Bound on Aerosol Radiative Forcing." J. Clim. 30, 6579–6584.
930 https://doi.org/10.1175/JCLI-D-16-0668.1
931 Lamarque, J.-F., Bond, T.C., Eyring, V., Granier, C., Heil, A., Klimont, Z., Lee, D., Liousse, C.,
932 Mieville, A., Owen, B., Schultz, M.G., Shindell, D., Smith, S.J., Stehfest, E., Van
933 Aardenne, J., Cooper, O.R., Kainuma, M., Mahowald, N., McConnell, J.R., Naik, V., Riahi,
934 K., van Vuuren, D.P., 2010. Historical (1850-2000) gridded anthropogenic and
935 biomass burning emissions of reactive gases and aerosols: methodology and
936 application. Atmospheric Chem. Phys. 10, 7017–7039. https://doi.org/10.5194/acp-
937 10-7017-2010
938 Latif, M., Boening, C., Willebrand, J., Biastoch, A., Dengg, J., Keenlyside, N., Schweckendiek,
939 U., Madec, G., 2006. Is the thermohaline circulation changing? J. Clim. 19, 4631–
940 4637. https://doi.org/10.1175/JCLI3876.1
941 Liu, W., Xie, S.-P., Liu, Z., Zhu, J., 2017. Overlooked possibility of a collapsed Atlantic
942 Meridional Overturning Circulation in warming climate. Sci. Adv. 3, e1601666.
943 https://doi.org/10.1126/sciadv.1601666
944 Liu, Y., Chiang, J.C.H., 2012. Coordinated Abrupt Weakening of the Eurasian and North
945 African Monsoons in the 1960s and Links to Extratropical North Atlantic Cooling. J.
946 Clim. 25, 3532–3548. https://doi.org/10.1175/JCLI-D-11-00219.1
947 Maher, N., Gupta, A.S., England, M.H., 2014. Drivers of decadal hiatus periods in the 20th
948 and 21st centuries. Geophys. Res. Lett. 41, 5978–5986.
949 https://doi.org/10.1002/2014GL060527
950 Mantsis, D., Clement, A., 2009. Simulated variability in the mean atmospheric meridional
951 circulation over the 20th century. Geophys. Res. Lett. 36.
952 https://doi.org/10.1029/2008GL036741
953 Mantua, N.J., Hare, S.R., Zhang, Y., Wallace, J.M., Francis, R.C., 1997. A Pacific Interdecadal
954 Climate Oscillation with Impacts on Salmon Production*. Bull. Am. Meteorol. Soc. 78,
955 1069–1080. https://doi.org/10.1175/1520-
956 0477(1997)078<1069:APICOW>2.0.CO;2
957 Marotzke, J., Forster, P.M., 2015. Forcing, feedback and internal variability in global
958 temperature trends. Nature 517, 565–570. https://doi.org/10.1038/nature14117
959 Marshall, J., Armour, K.C., Scott, J.R., Kostov, Y., Hausmann, U., Ferreira, D., Shepherd, T.G.,
960 Bitz, C.M., 2014. The ocean's role in polar climate change: asymmetric Arctic and
961 Antarctic responses to greenhouse gas and ozone forcing. Philos. Trans. R. Soc. Math.
962 Phys. Eng. Sci. 372, 20130040. https://doi.org/10.1098/rsta.2013.0040
963 Medhaug, I., Stolpe, M.B., Fischer, E.M., Knutti, R., 2017. Reconciling controversies about the
964 'global warming hiatus.' Nature 545, 41–47. https://doi.org/10.1038/nature22315
965 Meehl, G.A., Arblaster, J.M., Fasullo, J.T., Hu, A., Trenberth, K.E., 2011. Model-based evidence
966 of deep-ocean heat uptake during surface-temperature hiatus periods. Nat. Clim.
967 Change 1, 360–364. https://doi.org/10.1038/NCLIMATE1229
968 Menary, M.B., Hodson, D.L.R., Robson, J.I., Sutton, R.T., Wood, R.A., Hunt, J.A., 2015.
969 Exploring the impact of CMIP5 model biases on the simulation of North Atlantic
970 decadal variability. Geophys. Res. Lett. 42, 5926–5934.
971 https://doi.org/10.1002/2015GL064360
972 Moreno-Chamarro, E., Zanchettin, D., Lohmann, K., Jungclaus, J.H., 2015. Internally
973 generated decadal cold events in the northern North Atlantic and their possible

Accepted for publication in *Journal of Climate*. DOI 10.1175/JCLI-D-19-0102.1.

implications for the demise of the Norse settlements in Greenland. Geophys. Res. Lett. 2014GL062741. https://doi.org/10.1002/2014GL062741
Morice, C.P., Kennedy, J.J., Rayner, N.A., Jones, P.D., 2012. Quantifying uncertainties in global and regional temperature change using an ensemble of observational estimates: The HadCRUT4 data set. J. Geophys. Res. Atmospheres 1984–2012 117.
Muir, L.C., Fedorov, A.V., 2015. How the AMOC affects ocean temperatures on decadal to centennial timescales: the North Atlantic versus an interhemispheric seesaw. Clim. Dyn. 45, 151–160. https://doi.org/10.1007/s00382-014-2443-7
Neukom, R., Gergis, J., Karoly, D.J., Wanner, H., Curran, M., Elbert, J., González-Rouco, F., Linsley, B.K., Moy, A.D., Mundo, I., Raible, C.C., Steig, E.J., van Ommen, T., Vance, T., Villalba, R., Zinke, J., Frank, D., 2014. Inter-hemispheric temperature variability over the past millennium. Nat. Clim. Change 4, 362–367. https://doi.org/10.1038/nclimate2174
Neukom, R., Schurer, A.P., Steiger, N.J., Hegerl, G.C., 2018. Possible causes of data model discrepancy in the temperature history of the last Millennium. Sci. Rep. 8, 7572. https://doi.org/10.1038/s41598-018-25862-2
Overland, J., Rodionov, S.N., Minobe, S., Bond, N., 2008. North Pacific regime shifts: Definitions, issues and recent transitions. Prog. Oceanogr. 77, 92–102. https://doi.org/10.1016/j.pocean.2008.03.016
Park, T., Park, W., Latif, M., 2016. Correcting North Atlantic sea surface salinity biases in the Kiel Climate Model: influences on ocean circulation and Atlantic Multidecadal Variability. Clim. Dyn. 47, 2543–2560. https://doi.org/10.1007/s00382-016-2982-1
Parker, D., Folland, C., Scaife, A., Knight, J., Colman, A., Baines, P., Dong, B., 2007. Decadal to multidecadal variability and the climate change background. J. Geophys. Res. Atmospheres 112. https://doi.org/10.1029/2007JD008411
Polson, D., Bollasina, M., Hegerl, G.C., Wilcox, L.J., 2014. Decreased monsoon precipitation in the Northern Hemisphere due to anthropogenic aerosols. Geophys. Res. Lett. 41, 6023–6029. https://doi.org/10.1002/2014GL060811
Polson, D., Hegerl, G.C., Solomon, S., 2016. Precipitation sensitivity to warming estimated from long island records. Environ. Res. Lett. 11, 074024. https://doi.org/10.1088/1748-9326/11/7/074024
Power, S., Casey, T., Folland, C., Colman, A., Mehta, V., 1999. Inter-decadal modulation of the impact of ENSO on Australia. Clim. Dyn. 15, 319–324. https://doi.org/10.1007/s003820050284
Rahmstorf, S., Box, J.E., Feulner, G., Mann, M.E., Robinson, A., Rutherford, S., Schaffernicht, E.J., 2015. Exceptional twentieth-century slowdown in Atlantic Ocean overturning circulation. Nat. Clim. Change 5, 475–480. https://doi.org/10.1038/nclimate2554
Rajesh, R., Tiwari, R.K., 2018. Search for Trends and Periodicities in Inter-hemispheric Sea Surface Temperature Difference. Pure Appl. Geophys. 175, 2381–2394. https://doi.org/10.1007/s00024-018-1791-3
Reverdin, G., Friedman, A.R., Chafik, L., Holliday, N.P., Szekely, T., Valdimarsson, H., Yashayaev, I., 2019. North Atlantic extratropical and subpolar gyre variability during the last 120 years: a gridded dataset of surface temperature, salinity, and density. Part 1: dataset validation and RMS variability. Ocean Dyn. 69, 385–403. https://doi.org/10.1007/s10236-018-1240-y

Accepted for publication in *Journal of Climate*. DOI 10.1175/JCLI-D-19-0102.1.

1019 Rotstayn, L., Lohmann, U., 2002. Tropical rainfall trends and the indirect aerosol effect. J.
1020 Clim. 15, 2103–2116.
1021 Rotstayn, L.D., Collier, M.A., Chrastansky, A., Jeffrey, S.J., Luo, J.-J., 2013. Projected effects of
1022 declining aerosols in RCP4.5: unmasking global warming? Atmos Chem Phys 13,
1023 10883–10905. https://doi.org/10.5194/acp-13-10883-2013
1024 Rotstayn, L.D., Collier, M.A., Luo, J.-J., 2015. Effects of declining aerosols on projections of
1025 zonally averaged tropical precipitation. Environ. Res. Lett. 10, 044018.
1026 https://doi.org/10.1088/1748-9326/10/4/044018
1027 Saba, V.S., Griffies, S.M., Anderson, W.G., Winton, M., Alexander, M.A., Delworth, T.L., Hare,
1028 J.A., Harrison, M.J., Rosati, A., Vecchi, G.A., Zhang, R., 2016. Enhanced warming of the
1029 Northwest Atlantic Ocean under climate change. J. Geophys. Res. Oceans 121, 118–
1030 132. https://doi.org/10.1002/2015JC011346
1031 Santer, B.D., Wigley, T.M.L., Boyle, J.S., Gaffen, D.J., Hnilo, J.J., Nychka, D., Parker, D.E., Taylor,
1032 K.E., 2000. Statistical significance of trends and trend differences in layer-average
1033 atmospheric temperature time series. J. Geophys. Res. Atmospheres 105, 7337–
1034 7356. https://doi.org/10.1029/1999JD901105
1035 Schneider, T., Bischoff, T., Haug, G.H., 2014. Migrations and dynamics of the intertropical
1036 convergence zone. Nature 513, 45–53. https://doi.org/10.1038/nature13636
1037 Schneider, U., Becker, A., Finger, P., Meyer-Christoffer, A., Ziese, M., 2018. GPCC Full Data
1038 Monthly Version 2018.0 at 2.5°: Monthly Land-Surface Precipitation from Rain-
1039 Gauges built on GTS-based and Historic Data.
1040 https://doi.org/10.5676/dwd_gpcc/fd_m_v2018_250
1041 Schurer, A., Hegerl, G., Ribes, A., Polson, D., Morice, C., Tett, S., 2018. Estimating the
1042 Transient Climate Response from Observed Warming. J. Clim. 31, 8645–8663.
1043 https://doi.org/10.1175/JCLI-D-17-0717.1
1044 Schurer, A.P., Hegerl, G.C., Mann, M.E., Tett, S.F.B., Phipps, S.J., 2013. Separating Forced from
1045 Chaotic Climate Variability over the Past Millennium. J. Clim. 26, 6954–6973.
1046 https://doi.org/10.1175/JCLI-D-12-00826.1
1047 Schurer, A.P., Hegerl, G.C., Obrochta, S.P., 2015. Determining the likelihood of pauses and
1048 surges in global warming. Geophys. Res. Lett. 42, 2015GL064458.
1049 https://doi.org/10.1002/2015GL064458
1050 Schurer, A.P., Tett, S.F.B., Hegerl, G.C., 2014. Small influence of solar variability on climate
1051 over the past millennium. Nat. Geosci. 7, 104–108.
1052 https://doi.org/10.1038/ngeo2040
1053 Sen Gupta, A., Jourdain, N.C., Brown, J.N., Monselesan, D., 2013. Climate Drift in the CMIP5
1054 Models. J. Clim. 26, 8597–8615. https://doi.org/10.1175/JCLI-D-12-00521.1
1055 Serreze, M.C., Barry, R.G., 2011. Processes and impacts of Arctic amplification: A research
1056 synthesis. Glob. Planet. Change 77, 85–96.
1057 https://doi.org/10.1016/j.gloplacha.2011.03.004
1058 Servain, J., Wainer, I., McCreary, J.P., Dessier, A., 1999. Relationship between the equatorial
1059 and meridional modes of climatic variability in the tropical Atlantic. Geophys. Res.
1060 Lett. 26, 485–488. https://doi.org/10.1029/1999GL900014
1061 Sgubin, G., Swingedouw, D., Drijfhout, S., Mary, Y., Bennabi, A., 2017. Abrupt cooling over
1062 the North Atlantic in modern climate models. Nat. Commun. 8.
1063 https://doi.org/10.1038/ncomms14375

Accepted for publication in *Journal of Climate*. DOI 10.1175/JCLI-D-19-0102.1.

1064 Stevens, B., 2015. Rethinking the Lower Bound on Aerosol Radiative Forcing. J. Clim. 28,
1065 4794–4819. https://doi.org/10.1175/JCLI-D-14-00656.1
1066 Stouffer, R., Manabe, S., Bryan, K., 1989. Interhemispheric Asymmetry In Climate Response
1067 To A Gradual Increase Of Atmospheric CO2. Nature 342, 660–662.
1068 Stouffer, R.J., Seidov, D., Haupt, B.J., 2007. Climate Response to External Sources of
1069 Freshwater: North Atlantic versus the Southern Ocean. J. Clim. 20, 436–448.
1070 https://doi.org/10.1175/JCLI4015.1
1071 Sun, C., Li, J., Jin, F.-F., Ding, R., 2013. Sea surface temperature inter-hemispheric dipole and
1072 its relation to tropical precipitation. Environ. Res. Lett. 8, 044006.
1073 https://doi.org/10.1088/1748-9326/8/4/044006
1074 Sun, C., Li, J., Li, X., Xue, J., Ding, R., Xie, F., Li, Y., 2018. Oceanic forcing of the
1075 interhemispheric SST dipole associated with the Atlantic Multidecadal Oscillation.
1076 Environ. Res. Lett. 13, 074026. https://doi.org/10.1088/1748-9326/aacf66
1077 Swingedouw, D., Mignot, J., Labetoulle, S., Guilyardi, E., Madec, G., 2013. Initialisation and
1078 predictability of the AMOC over the last 50 years in a climate model. Clim. Dyn. 40,
1079 2381–2399. https://doi.org/10.1007/s00382-012-1516-8
1080 Swingedouw, D., Mignot, J., Ortega, P., Khodri, M., Menegoz, M., Cassou, C., Hanquiez, V.,
1081 2017. Impact of explosive volcanic eruptions on the main climate variability modes.
1082 Glob. Planet. Change 150, 24–45. https://doi.org/10.1016/j.gloplacha.2017.01.006
1083 Taylor, K.E., Stouffer, R.J., Meehl, G.A., 2012. An Overview of CMIP5 and the Experiment
1084 Design. Bull. Am. Meteorol. Soc. 93, 485–498. https://doi.org/10.1175/BAMS-D-11-
1085 00094.1
1086 Terray, L., 2012. Evidence for multiple drivers of North Atlantic multi-decadal climate
1087 variability. Geophys. Res. Lett. 39. https://doi.org/10.1029/2012GL053046
1088 Tett, S.F.B., Jones, G.S., Stott, P.A., Hill, D.C., Mitchell, J.F.B., Allen, M.R., Ingram, W.J., Johns,
1089 T.C., Johnson, C.E., Jones, A., Roberts, D.L., Sexton, D.M.H., Woodage, M.J., 2002.
1090 Estimation of natural and anthropogenic contributions to twentieth century
1091 temperature change. J. Geophys. Res. Atmospheres 107, ACL 10-1-ACL 10-24.
1092 https://doi.org/10.1029/2000JD000028
1093 Thibodeau, B., Not, C., Zhu, J., Schmittner, A., Noone, D., Tabor, C., Zhang, J., Liu, Z., 2018. Last
1094 Century Warming Over the Canadian Atlantic Shelves Linked to Weak Atlantic
1095 Meridional Overturning Circulation. Geophys. Res. Lett. 45, 12,376-12,385.
1096 https://doi.org/10.1029/2018GL080083
1097 Thompson, D.W.J., Wallace, J.M., Jones, P.D., Kennedy, J.J., 2009. Identifying Signatures of
1098 Natural Climate Variability in Time Series of Global-Mean Surface Temperature:
1099 Methodology and Insights. J. Clim. 22, 6120–6141.
1100 https://doi.org/10.1175/2009JCLI3089.1
1101 Thompson, D.W.J., Wallace, J.M., Kennedy, J.J., Jones, P.D., 2010. An abrupt drop in Northern
1102 Hemisphere sea surface temperature around 1970. Nature 467, 444–447.
1103 https://doi.org/10.1038/nature09394
1104 Thornalley, D.J.R., Oppo, D.W., Ortega, P., Robson, J.I., Brierley, C.M., Davis, R., Hall, I.R.,
1105 Moffa-Sanchez, P., Rose, N.L., Spooner, P.T., Yashayaev, I., Keigwin, L.D., 2018.
1106 Anomalously weak Labrador Sea convection and Atlantic overturning during the
1107 past 150 years. Nature 556, 227. https://doi.org/10.1038/s41586-018-0007-4

Accepted for publication in *Journal of Climate*. DOI 10.1175/JCLI-D-19-0102.1.

1108 Trottini, M., Isabel, M., Aguiar, V., Palazón, S.B., 2015. On the Use of Running Trends as
1109 Summary Statistics for Univariate Time Series and Time Series Association. J. Clim.
1110 28, 7489–7502. https://doi.org/10.1175/JCLI-D-15-0009.1
1111 Undorf, S., Polson, D., Bollasina, M.A., Ming, Y., Schurer, A., Hegerl, G.C., 2018. Detectable
1112 Impact of Local and Remote Anthropogenic Aerosols on the 20th Century Changes of
1113 West African and South Asian Monsoon Precipitation. J. Geophys. Res.-
1114 ATMOSPHERES 123, 4871–4889. https://doi.org/10.1029/2017JD027711
1115 Vellinga, M., Wu, P., 2004. Low-Latitude Freshwater Influence on Centennial Variability of
1116 the Atlantic Thermohaline Circulation. J. Clim. 17, 4498–4511.
1117 https://doi.org/10.1175/3219.1
1118 Vuuren, D.P. van, Edmonds, J., Kainuma, M., Riahi, K., Thomson, A., Hibbard, K., Hurtt, G.C.,
1119 Kram, T., Krey, V., Lamarque, J.-F., Masui, T., Meinshausen, M., Nakicenovic, N., Smith,
1120 S.J., Rose, S.K., 2011. The representative concentration pathways: an overview. Clim.
1121 Change 109, 5–31. https://doi.org/10.1007/s10584-011-0148-z
1122 Wang, B., Liu, J., Kim, H.-J., Webster, P.J., Yim, S.-Y., 2012. Recent change of the global
1123 monsoon precipitation (1979-2008). Clim. Dyn. 39, 1123–1135.
1124 https://doi.org/10.1007/s00382-011-1266-z
1125 Wang, R., Balkanski, Y., Boucher, O., Ciais, P., Schuster, G.L., Chevallier, F., Samset, B.H., Liu,
1126 J., Piao, S., Valari, M., Tao, S., 2016. Estimation of global black carbon direct radiative
1127 forcing and its uncertainty constrained by observations. J. Geophys. Res.
1128 Atmospheres 121, 5948–5971. https://doi.org/10.1002/2015JD024326
1129 Wang, Z., Zhang, X., Guan, Z., Sun, B., Yang, X., Liu, C., 2015. An atmospheric origin of the
1130 multi-decadal bipolar seesaw. Sci. Rep. 5, 8909. https://doi.org/10.1038/srep08909
1131 Wilcox, L.J., Highwood, E.J., Dunstone, N.J., 2013. The influence of anthropogenic aerosol on
1132 multi-decadal variations of historical global climate. Environ. Res. Lett. 8, 024033.
1133 https://doi.org/10.1088/1748-9326/8/2/024033
1134 Wilks, D.S., 2016. "The Stippling Shows Statistically Significant Grid Points": How Research
1135 Results are Routinely Overstated and Overinterpreted, and What to Do about It. Bull.
1136 Am. Meteorol. Soc. 97, 2263–2273. https://doi.org/10.1175/BAMS-D-15-00267.1
1137 Xie, S.-P., 2016. Oceanography: Leading the hiatus research surge. Nat. Clim. Change 6, 345–
1138 346. https://doi.org/10.1038/nclimate2973
1139 Xie, S.P., Carton, J.A., 2004. Tropical Atlantic variability: Patterns, mechanisms, and impacts,
1140 in: Earth's Climate: The Ocean-Atmosphere Interaction, Geophys. Monogr,
1141 Geophysical Monograph Series. pp. 121–142.
1142 Xu, Y., Ramanathan, V., 2012. Latitudinally asymmetric response of global surface
1143 temperature: Implications for regional climate change. Geophys. Res. Lett. 39.
1144 https://doi.org/10.1029/2012GL052116
1145 Xue, J., Sun, C., Li, J., Mao, J., Nakamura, H., Miyasaka, T., Xu, Y., 2018. Divergent Responses of
1146 Extratropical Atmospheric Circulation to Interhemispheric Dipolar SST Forcing over
1147 the Two Hemispheres in Boreal Winter. J. Clim. 31, 7599–7619.
1148 https://doi.org/10.1175/JCLI-D-17-0817.1
1149 Yan, X.-H., Boyer, T., Trenberth, K., Karl, T.R., Xie, S.-P., Nieves, V., Tung, K.-K., Roemmich, D.,
1150 2016. The global warming hiatus: Slowdown or redistribution? Earths Future 4,
1151 472–482. https://doi.org/10.1002/2016EF000417

Accepted for publication in *Journal of Climate*. DOI 10.1175/JCLI-D-19-0102.1.

Zhang, R., Delworth, T.L., 2007. Impact of the Atlantic Multidecadal Oscillation on North Pacific climate variability. Geophys. Res. Lett. 34, L23708. https://doi.org/10.1029/2007GL031601

Zhang, Y., Wallace, J.M., Battisti, D.S., 1997. ENSO-like Interdecadal Variability: 1900–93. J. Clim. 10, 1004–1020. https://doi.org/10.1175/1520-0442(1997)010<1004:ELIV>2.0.CO;2

Accepted for publication in *Journal of Climate*. DOI 10.1175/JCLI-D-19-0102.1.

Table 1: Models investigated. CMIP5 groups and models are listed with the number of historical and historicalNat realizations; the length of the piControl simulations; and the number of 132-year segments from the control simulations used in the analysis.

		Historical, HistoricalNat	piControl	
Group	**Model**	**Realizations**	**length (yrs.)**	**segments**
BCC	bcc-csm1-1	1	500	3
CCCma	CanESM2	5	996	7
CNRM-CERFACS	CNRM-CM5	6	850	6
CSIRO-QCCCE	CSIRO-Mk3-6-0	5	500	3
IPSL	IPSL-CM5A-LR	3	1000	7
IPSL	IPSL-CM5A-MR	1	300	2
MOHC	HadGEM2-ES	4	576	4
NASA-GISS	GISS-E2-H	5	540	4
NASA-GISS	GISS-E2-R	5	500	3
NCC	NorESM1-M	1	501	3
NCAR	CCSM4		1051	7
NOAA-GFDL	GFDL-CM3		500	3

Accepted for publication in *Journal of Climate*. DOI 10.1175/JCLI-D-19-0102.1.

Table 2: Detection and attribution scaling factors. Best-estimate scaling factors and 5-95% confidence intervals for natural (left) and anthropogenic (right) forcing for the (a) interhemispheric SST contrast and (b) NH and SH individually. Bold coefficients are detected at a 95% significance level, and asterisks indicate where the confidence intervals are outside the multimodel mean.

(a) NH–SH

	β_{Nat}	β_{Ant}
HadSST3:	1.14 (–0.3 to 2.2)	**1.32** (0.7 to 2.6)
ERSSTv5:	0.30 (–1.2 to 1.4)	**1.90** (1.2 to 3.3) *

(b) NH and SH

NH	β_{Nat}	β_{Ant}
HadSST3:	**0.57** (0.1 to 1.0)	**1.13** (0.8 to 1.5)
ERSSTv5:	0.28 (–0.2 to 0.7)	**1.20** (0.9 to 1.5)
SH		
HadSST3:	**0.40** (+0.0 to 0.7) *	**1.19** (1.1 to 1.4) *
ERSSTv5:	–0.22 (–0.6 to 0.1)	**1.32** (1.2 to 1.5) *

Accepted for publication in *Journal of Climate*. DOI 10.1175/JCLI-D-19-0102.1.

Table 3. 1970 and 1920s trend magnitudes. 9-year observational and best-estimate residual SST trend magnitudes over 1966–1974 and 1918–1926 for the interhemispheric SST contrast, the NH, and the SH, in °C per decade.

	Observations		Best-estimate residual	
1966–1974	**HadSST3**	**ERSSTv5**	**HadSST3**	**ERSSTv5**
NH-SH	–0.61	–0.64	–0.53	–0.49
NH	–0.34	–0.25	–0.40	–0.27
SH	0.27	0.40	0.15	0.34
1918–1926	**HadSST3**	**ERSSTv5**	**HadSST3**	**ERSSTv5**
NH-SH	0.42	0.30	0.40	0.21
NH	0.29	0.17	0.22	0.08
SH	–0.13	–0.12	–0.17	–0.18

Accepted for publication in *Journal of Climate*. DOI 10.1175/JCLI-D-19-0102.1.

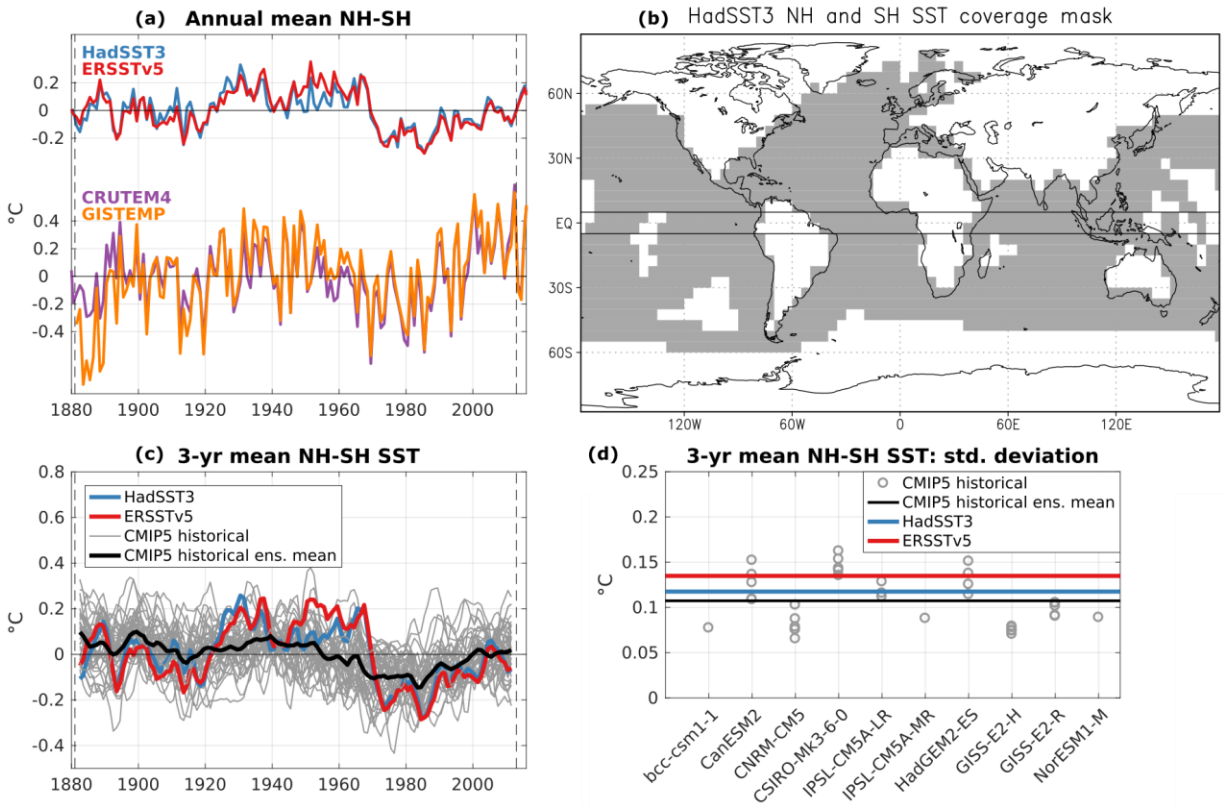

Figure 1. Interhemispheric temperature and SST contrast time series. (a) Top: annual mean (December–November) interhemispheric SST contrast anomaly of HadSST3 (blue) and ERSSTv5 (red). Bottom: land surface interhemispheric contrast anomaly of CRUTEM4 (purple) and GISTEMP (orange). Anomalies are from 1881-2012 (vertical dashed lines). (b) Gridpoints included in computing the northern and southern hemisphere SST means, based on HadSST3 data coverage and poleward of 5° latitude (solid lines). (c) 3-year running mean interhemispheric SST contrast anomaly of CMIP5 historical realizations and observations. Thin lines show individual realizations; the solid black line shows the multimodel ensemble mean. (d) 1881–2012 standard deviations of the 3-year mean interhemispheric SST contrast of observations and historical realizations from (c). Grey circles show individual realizations; the solid black line shows the multimodel ensemble mean.

Accepted for publication in *Journal of Climate*. DOI 10.1175/JCLI-D-19-0102.1.

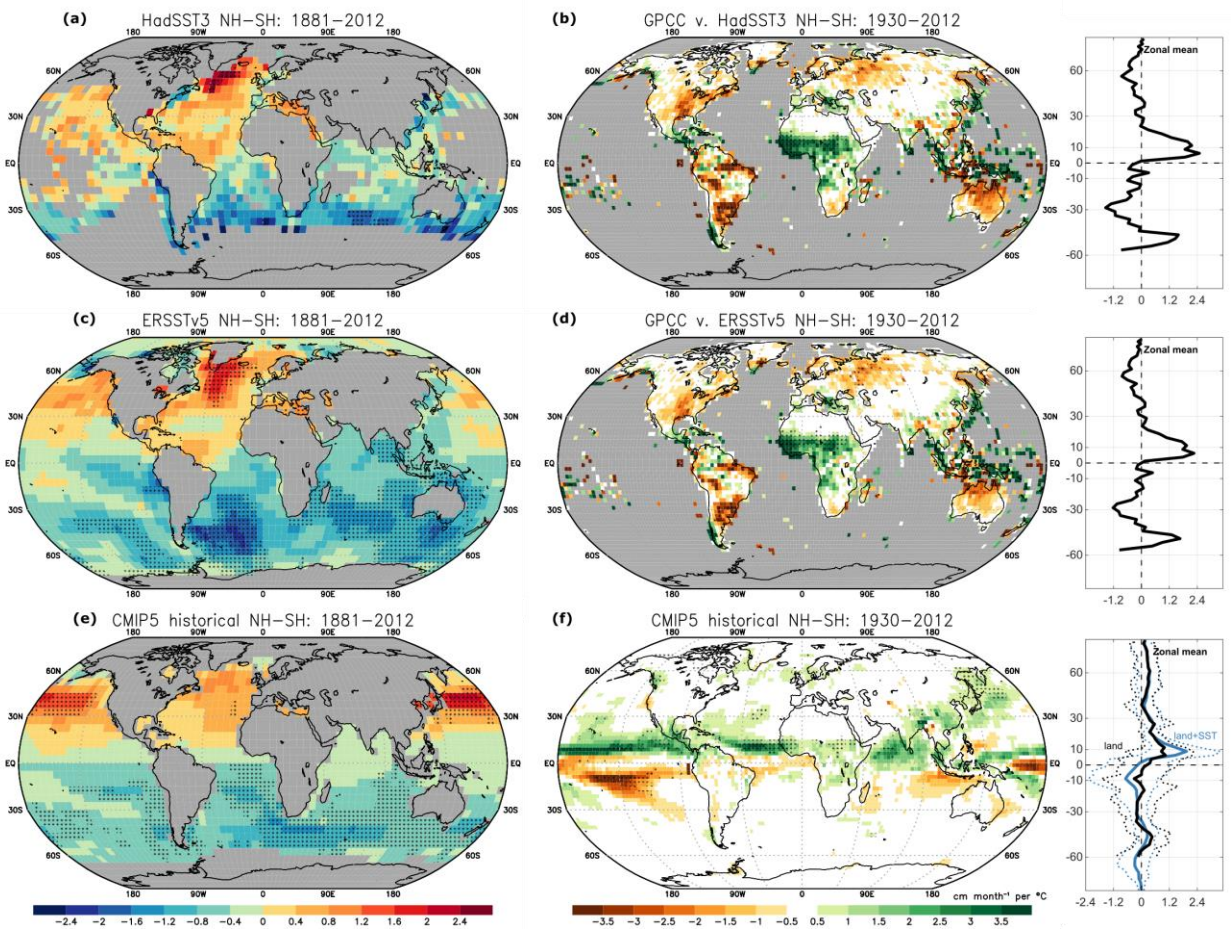

Figure 2. Interhemispheric SST contrast spatial patterns: SST and rainfall. (a, c, e) Slope of 3-year mean SST v. interhemispheric SST contrast from 1881-2012 (from **Figure 1c**) for (a) HadSST3, (c) ERSSTv5, and (e) CMIP5 historical ensemble mean, in °C per °C (unitless). (b, d, f) Slope of 3-year mean precipitation v. interhemispheric SST contrast for (b) GPCC rainfall and HadSST3 from 1930–2012, (d) GPCC rainfall and ERSSTv5 from 1930–2012, and (f) CMIP5 historical mean from 1930–2012, in cm month^{-1} per °C. Right panels show the zonal mean slopes. Stippling in (a)–(d) indicates where the slope is significant at $p<0.05$ and satisfying $\alpha_{FDR} = 0.05$ (see text). Stippling in (e) and (f) indicates sign agreement of at least 30 out of 36 realizations. Colors in the right panel of (f) indicate land + SST (blue) and land only (black) slopes; dotted lines enclose the middle 30 out of 36 realizations.

Accepted for publication in *Journal of Climate*. DOI 10.1175/JCLI-D-19-0102.1.

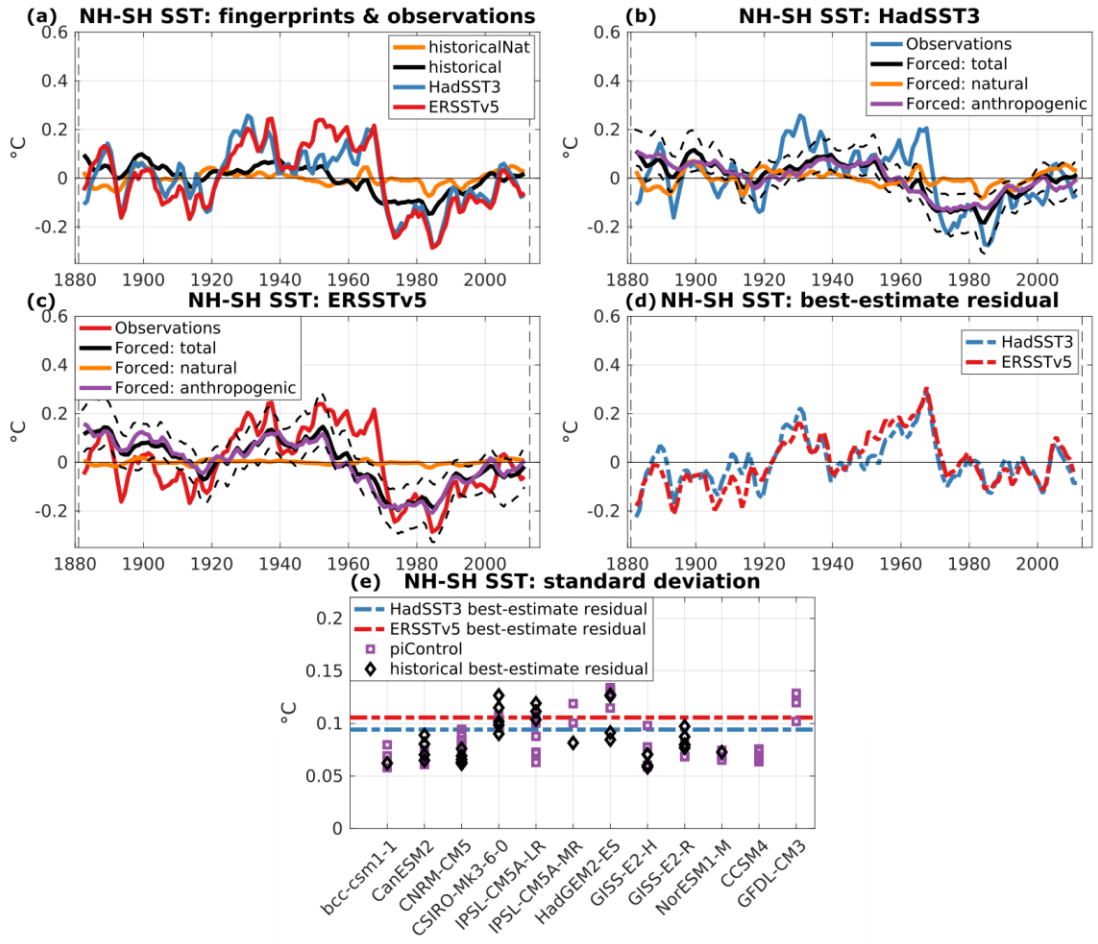

Figure 3. Interhemispheric SST contrast detection and attribution. (a) 3-year mean interhemispheric SST contrast anomaly: historicalNat and historical fingerprints, and observations. (b-c) Forced component of the interhemispheric SST contrast for (b) HadSST3 and (c) ERSSTv5. Thick black line is the best-estimate forced component; thin dashed lines indicate the 5-95% confidence intervals (see text). The components from anthropogenic and natural forcing are also shown. (d) Best-estimate residual interhemispheric SST contrast time series for HadSST3 and ERSSTv5. (e) Standard deviations of the best-estimate observational residuals, control simulations, and best-estimate historical realization residuals.

Accepted for publication in *Journal of Climate*. DOI 10.1175/JCLI-D-19-0102.1.

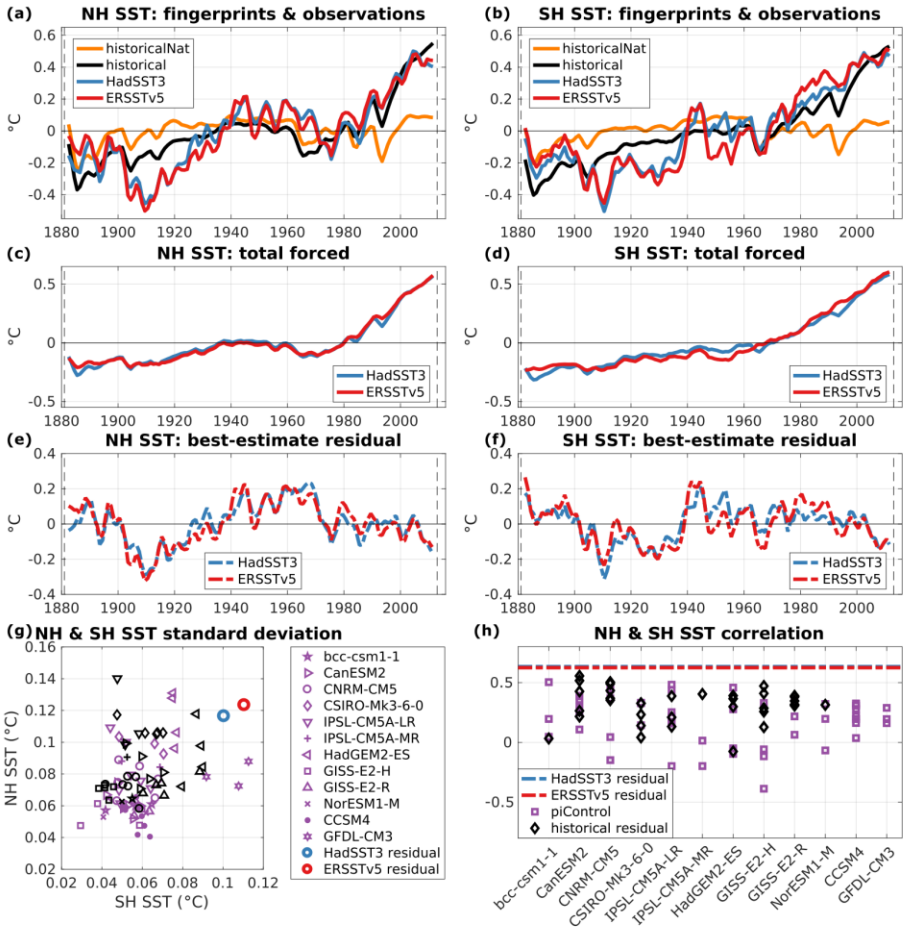

Figure 4. Separate northern and southern hemisphere SST detection and attribution. (a-b) 3-year mean (a) NH and (b) SH SST anomalies: historicalNat and historical fingerprints, and observations. (c-d) Total forced component of the (c) NH and (d) SH SST. (e-f) Best-estimate residual SST time series for the (e) NH and (f) SH. (g) Standard deviations of NH and SH SST from best-estimate observational residuals, control simulations, and best-estimate historical realization residuals. Purple markers show the control simulations, and black markers show the best-estimate historical simulation residuals. (h) Correlations of best-estimate residual NH and SH SST with those of control simulations and best-estimate historical simulation residuals.

Accepted for publication in *Journal of Climate*. DOI 10.1175/JCLI-D-19-0102.1.

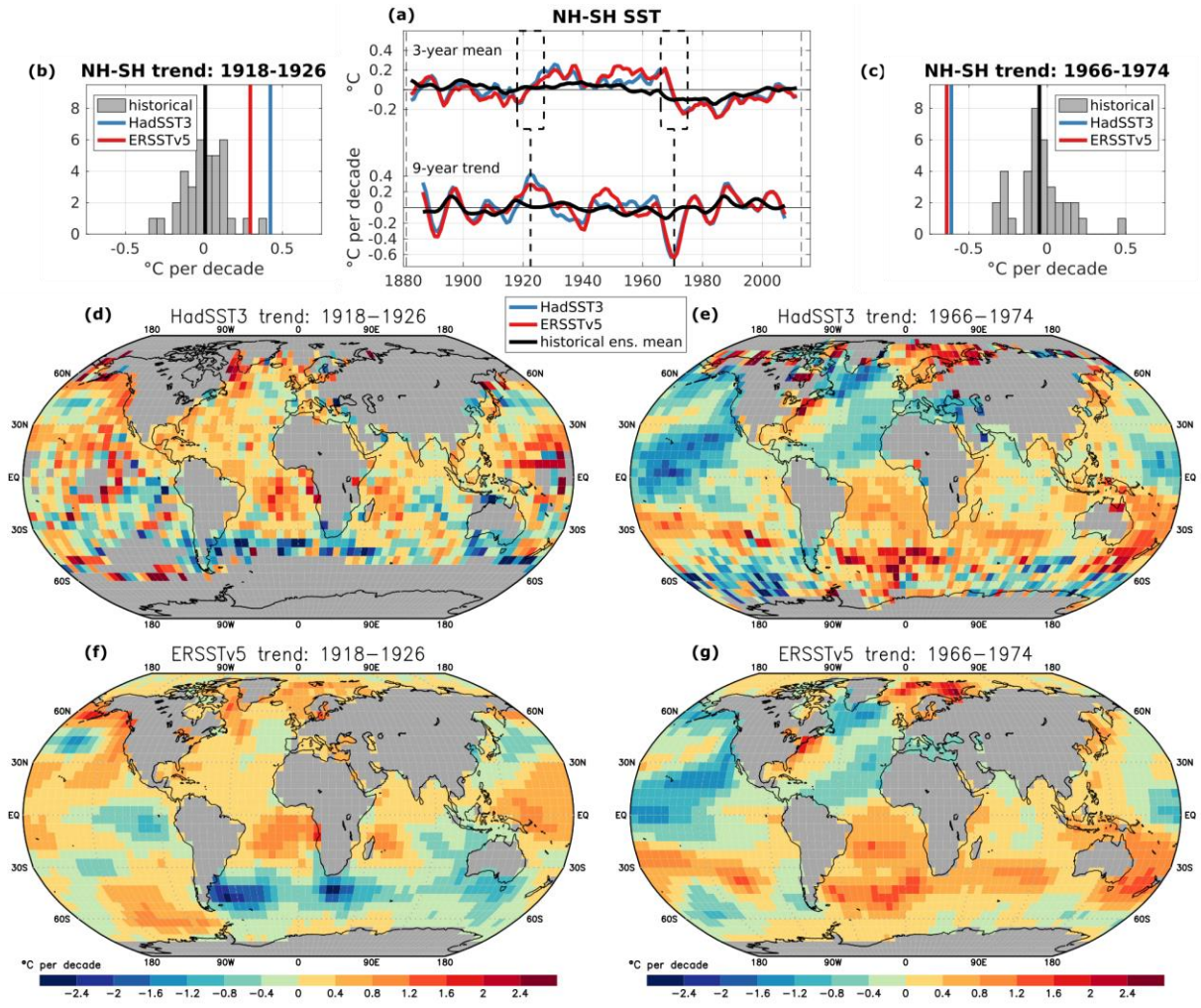

Figure 5. Early-1920s and 1970 interhemispheric SST shifts. (a) Top: 3-year mean interhemispheric SST contrast anomaly for HadSST3 (blue), ERSSTv5 (red), and CMIP5 historical multimodel ensemble mean (black), in °C. Bottom: 9-year running mean trends, in °C per decade. The dashed vertical lines indicate the trends centered in 1922 and 1970. (b–c) Distribution of 9-year interhemispheric SST trends of each CMIP5 historical realization compared with observations for (b) 1918–1926 and (c) 1966–1974. The multimodel ensemble mean is shown as a solid black line. (d, f) 9-year SST trend for the period centered in 1922 for (d) HadSST3 and (f) ERSSTv5, in °C per decade. (e, g) Same as (d, f), but for the trend centered in 1970.

Accepted for publication in *Journal of Climate*. DOI 10.1175/JCLI-D-19-0102.1.

1261

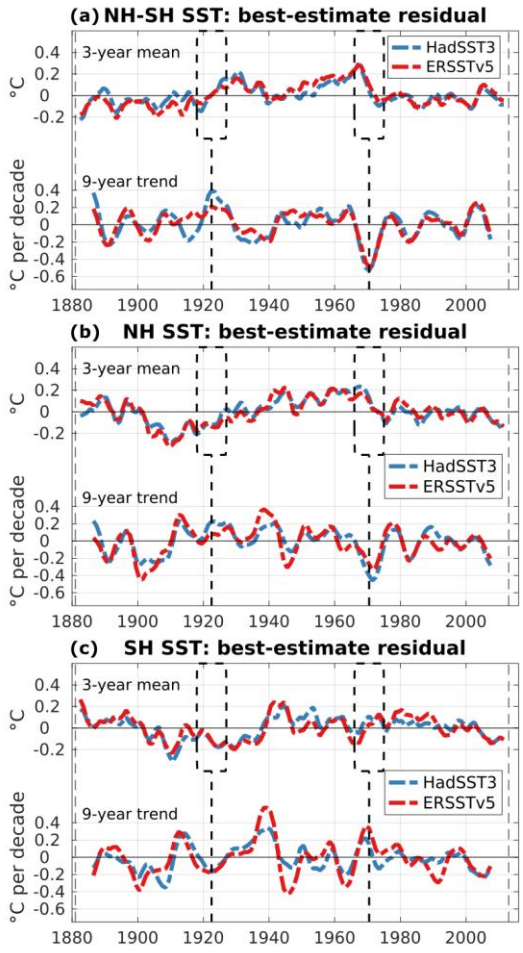

1262

1263 **Figure 6. Best-estimate residual SST running trends.** (a) 3-year mean best-estimate residual

1264 interhemispheric SST contrast for HadSST3 and ERSSTv5 in °C (top), with 9-year running

1265 mean trends in °C per decade (bottom). The dashed vertical lines indicate the trends centered in

1266 1922 and 1970. (b-c) Same as (a), but for the (b) NH (c) SH SST.

Accepted for publication in *Journal of Climate*. DOI 10.1175/JCLI-D-19-0102.1.

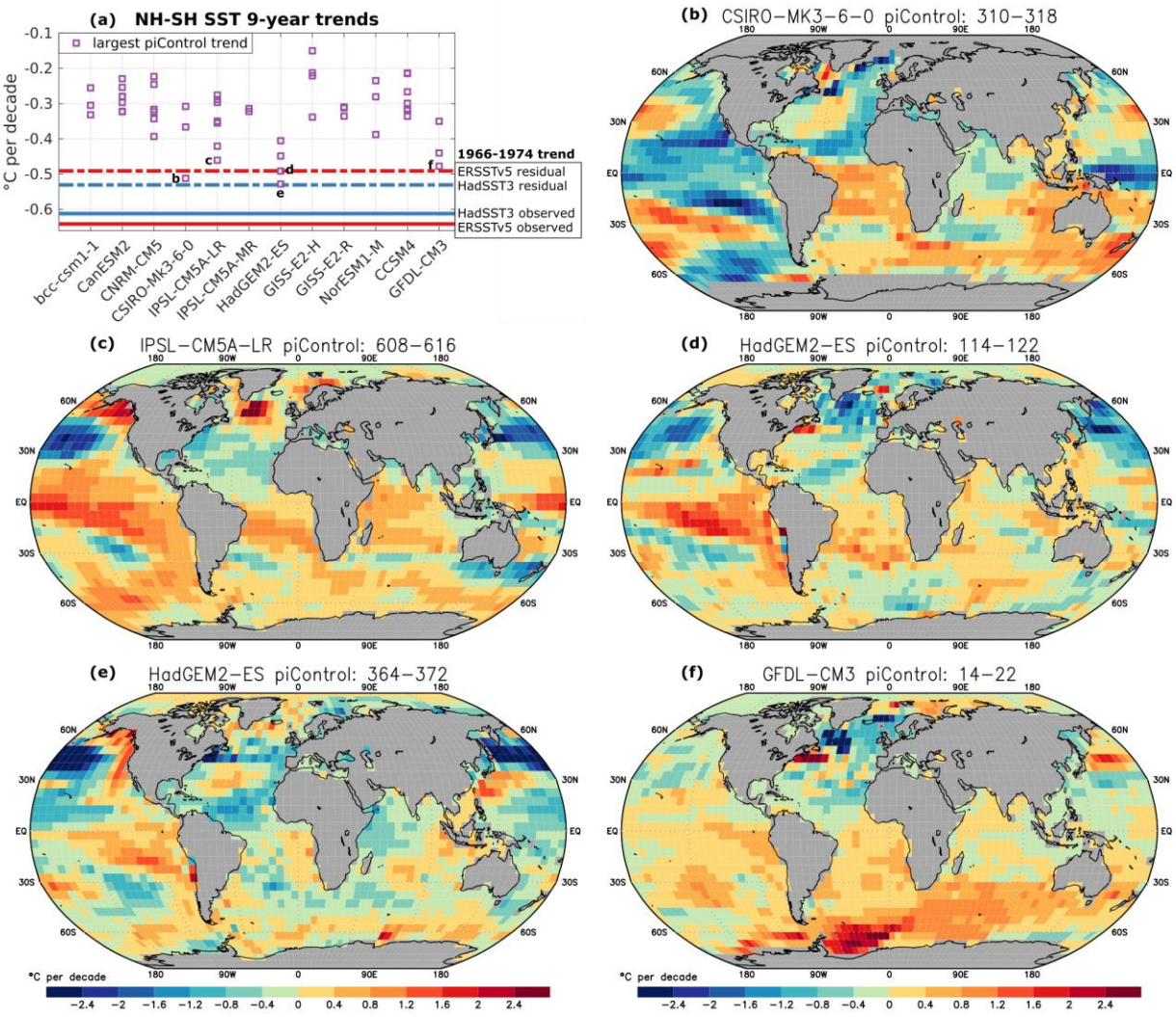

1267

1268 **Figure 7. Control simulation interhemispheric SST shifts**. (a) Comparison of the observed

1269 and best-estimate residual interhemispheric SST trends from 1966–1974 with the largest-

1270 magnitude negative (SH–NH) 9-yr interhemispheric SST trend in each control segment, in °C

1271 per decade. (b-f) Spatial patterns of the largest-magnitude control segment trends, indicated by

1272 small letters in (a), in °C per decade: (b) CSIRO-Mk3-6-0 years 310–318, (c) IPSL-CM5A-LR

1273 years 608–616, (d) HadGEM2-ES years 114–122, (e) HadGEM2-ES years 364–372, and (f)

1274 GFDL-CM3 years 14–22.

Accepted for publication in *Journal of Climate*. DOI 10.1175/JCLI-D-19-0102.1.

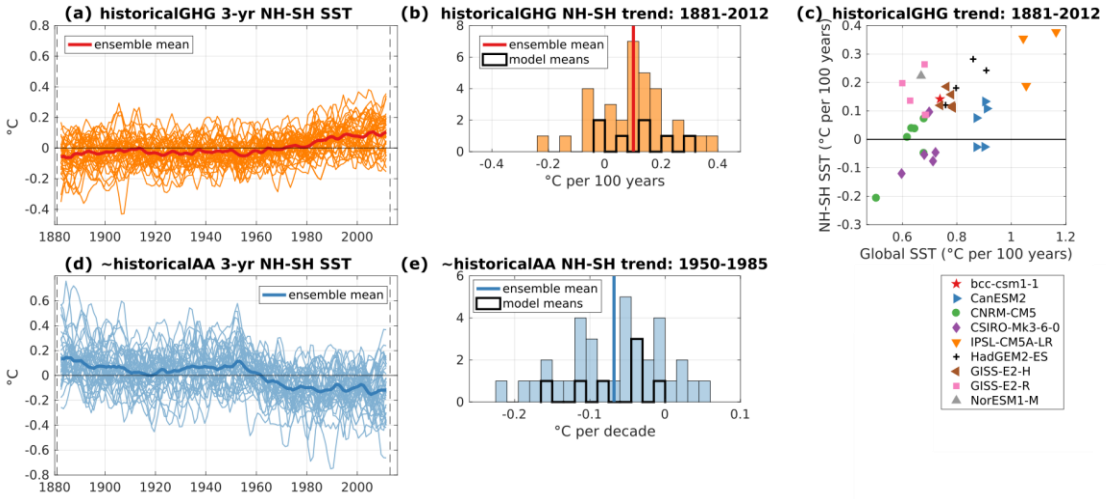

1275

1276 **Figure 8**. **Specific-forcing interhemispheric SST time series.** (a) 3-year running mean
1277 historicalGHG interhemispheric SST contrast anomaly time series of 35 realizations. Thin lines
1278 show individual realizations; the thick red line shows the multi-model ensemble mean. (b)
1279 Distribution of 1881–2012 trends of each realization in (a). Individual model realizations are
1280 shaded orange; model means are outlined in black. The thick red line indicates the multimodel
1281 ensemble mean. (c) 1881-2012 interhemispheric SST contrast trends from (b) v. the respective
1282 1881-2012 global mean SST trends. (d) 3-year running mean historicalAA interhemispheric SST
1283 contrast anomaly approximation (historical–historicalGHG–historicalNat) of 35 realizations.
1284 Thin lines show individual realizations; thick line shows the multimodel ensemble mean. (e)
1285 Distribution of 1950–1985 trends of each realization in (d). Individual model realizations are
1286 shaded light blue; model means are outlined in black. The thick blue line indicates the
1287 multimodel ensemble mean.

1288

Accepted for publication in *Journal of Climate*. DOI 10.1175/JCLI-D-19-0102.1.

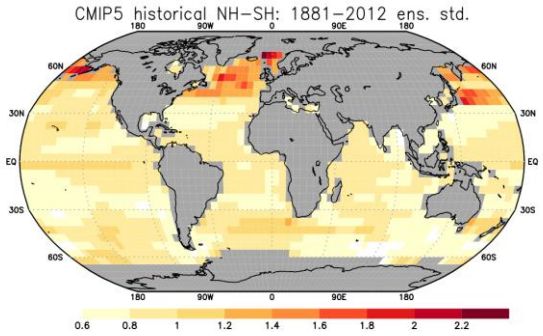

Figure 9. Inter-model interhemispheric SST spatial pattern variability. CMIP5 historical ensemble standard deviation of 3-year mean SST v. interhemispheric SST contrast from 1881-2012 (from **Figure 2e**), in °C per °C (unitless).

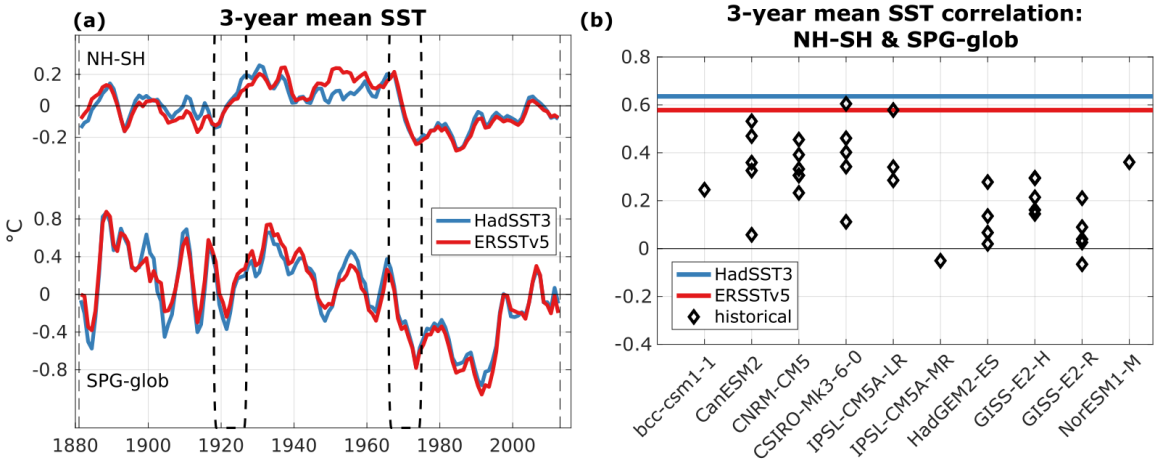

Figure 10. AMOC proxy SST index. (a) Observed 3-year running mean interhemispheric SST contrast anomaly (top) and AMOC proxy SST index (subpolar North Atlantic SST minus global mean SST) anomaly (bottom; note different scaling). (b) Correlations of the interhemispheric SST contrast and AMOC proxy SST index in observations and historical simulations.

Accepted for publication in *Journal of Climate*. DOI 10.1175/JCLI-D-19-0102.1.